

# Multiplexed screens identify RAS paralogues HRAS and NRAS as suppressors of KRAS-driven lung cancer growth

Received: 13 September 2021

Accepted: 9 November 2022

Published online: 12 January 2023

 Check for updates

Rui Tang<sup>1,10</sup>, Emily G. Shuldiner<sup>2,10</sup>, Marcus Kelly<sup>3,4</sup>, Christopher W. Murray<sup>3</sup>, Jess D. Hebert<sup>1</sup>, Laura Andrejka<sup>1</sup>, Min K. Tsai<sup>1,3</sup>, Nicholas W. Hughes<sup>1</sup>, Mitchell I. Parker<sup>5,6</sup>, Hongchen Cai<sup>1</sup>, Yao-Cheng Li<sup>7</sup>, Geoffrey M. Wahl<sup>7</sup>, Roland L. Dunbrack<sup>5</sup>, Peter K. Jackson<sup>3,4</sup>, Dmitri A. Petrov<sup>2,3,8</sup> & Monte M. Winslow<sup>1,3,9</sup> ✉

Oncogenic *KRAS* mutations occur in approximately 30% of lung adenocarcinoma. Despite several decades of effort, oncogenic *KRAS*-driven lung cancer remains difficult to treat, and our understanding of the regulators of RAS signalling is incomplete. Here to uncover the impact of diverse *KRAS*-interacting proteins on lung cancer growth, we combined multiplexed somatic CRISPR/Cas9-based genome editing in genetically engineered mouse models with tumour barcoding and high-throughput barcode sequencing. Through a series of CRISPR/Cas9 screens in autochthonous lung cancer models, we show that HRAS and NRAS are suppressors of *KRAS*<sup>G12D</sup>-driven tumour growth in vivo and confirm these effects in oncogenic *KRAS*-driven human lung cancer cell lines. Mechanistically, RAS paralogues interact with oncogenic *KRAS*, suppress *KRAS*–*KRAS* interactions, and reduce downstream ERK signalling. Furthermore, *HRAS* and *NRAS* mutations identified in oncogenic *KRAS*-driven human tumours partially abolished this effect. By comparing the tumour-suppressive effects of HRAS and NRAS in oncogenic *KRAS*- and oncogenic BRAF-driven lung cancer models, we confirm that RAS paralogues are specific suppressors of *KRAS*-driven lung cancer in vivo. Our study outlines a technological avenue to uncover positive and negative regulators of oncogenic *KRAS*-driven cancer in a multiplexed manner in vivo and highlights the role RAS paralogue imbalance in oncogenic *KRAS*-driven lung cancer.

The RAS family genes *KRAS*, *HRAS* and *NRAS* are frequently mutated across cancers, and *KRAS* mutations occur in approximately 30% of lung adenocarcinomas<sup>1–3</sup>. RAS proteins are small GTPases that switch between a GTP-bound active state and a GDP-bound inactive state in response to upstream growth factor signalling<sup>4</sup>. RAS proteins regulate multiple downstream signalling pathways that control proliferation. Oncogenic mutations in codons 12, 13 and 61 reduce GTP

hydrolysis and increase the fraction of RAS proteins in the GTP-bound state, which results in widespread changes in RAS protein–protein interactions<sup>5,6</sup>. This hyper-activation of RAS effector pathways culminates in cellular transformation and tumorigenesis<sup>7,8</sup>. Oncogenic *KRAS* therefore represents a key node in growth-factor-induced signalling and a critical target for therapeutic intervention in lung adenocarcinoma<sup>9</sup>.

A full list of affiliations appears at the end of the paper. ✉ e-mail: [mwinslow@stanford.edu](mailto:mwinslow@stanford.edu)

Genetic and proteomic mapping has revealed that KRAS interacts with a large network of proteins<sup>10,11</sup>. These KRAS-interacting proteins include canonical regulators and effectors, as well as many proteins that remain poorly understood in the context of oncogenic KRAS-driven lung cancer. Much of our understanding of RAS signalling stems from diverse cellular and cell-free systems<sup>12–14</sup>. Thus, while recent studies have mapped KRAS protein–protein interaction networks<sup>10,11,15,16</sup>, it remains difficult to assess the relevance of these interactions to cancer growth in vivo. Genetically engineered mouse models of oncogenic KRAS-driven cancer uniquely recapitulate autochthonous tumour growth and have contributed to our understanding of KRAS signalling<sup>17</sup>. However, the development and use of such models has traditionally been insufficiently scalable to broadly assess modifiers of KRAS-driven tumour growth. The ability to uncover functional components of RAS signalling that affect lung cancer growth in vivo in a multiplexed manner would accelerate our understanding of RAS biology and could aid in the development of pharmacological strategies to counteract hyperactivated KRAS.

To enable the analysis of genetic modifiers of lung tumour growth in vivo, we recently integrated somatic clustered regularly interspaced short palindromic repeats (CRISPR)/Cas9-based genome editing with tumour barcoding and high-throughput barcode sequencing (Tuba-seq)<sup>18–20</sup>. This approach allows precise quantification of the effects of inactivating panels of genes of interest on lung tumour initiation and growth in a multiplexed manner. By employing Tuba-seq to assess the functions of KRAS-interacting proteins nominated by unbiased affinity purification/mass spectrometry (AP/MS), we show that wild-type HRAS and NRAS suppress the growth of oncogenic KRAS-driven lung adenocarcinoma. Competition between oncogenic KRAS and wild-type HRAS and NRAS diminishes KRAS–KRAS interaction and suppresses downstream signalling. In vivo screening across multiple oncogenic contexts revealed that HRAS and NRAS specifically suppress the growth of tumours driven by oncogenic KRAS. Our study reveals that changes in the ratio of RAS paralogues (which we term ‘RAS paralogue imbalance’) is a driver of oncogenic KRAS-driven lung cancer.

## Results

### Selection of candidate KRAS-interacting proteins

To identify KRAS-interacting proteins that could affect oncogenic KRAS-driven lung tumour growth in vivo, we integrated pre-existing proteomic data from AP/MS studies with gene expression data from cancer cells from autochthonous mouse models (Fig. 1a)<sup>10,21</sup>. We prioritized a list of candidate genes according to the probability of their protein products interacting with KRAS and other RAS GTPases, as well as their messenger RNA expression in mouse models of oncogenic KRAS<sup>G12D</sup>-driven lung cancer (Fig. 1b,c and Extended Data Fig. 1a–d)<sup>10,21</sup>. We selected 13 proteins that represent diverse aspects of RAS biology, including RAS paralogues (HRAS and NRAS, which were supported by the identification of paralogue-specific peptides), RAS regulators (RAS-GRF2 and RAP1GDS1) (refs. 22,23), a RAS farnesyltransferase (FNTA)<sup>24,25</sup> and RAS effectors (RAF1, RGL2) (refs. 26,27), as well as several proteins whose functions in RAS signalling are understudied. While the majority of these candidate genes trend towards amplification in oncogenic KRAS-driven lung adenocarcinoma, *NRAS*, *HRAS* and *ALDH1A1* have deep genomic deletions (Extended Data Fig. 1e)<sup>28</sup>. Interestingly, some of these proteins bound preferentially to either GTP- or GDP-bound KRAS, while others interact with KRAS independently of its nucleotide state (Fig. 1c).

### KRAS-interacting proteins impact lung tumour growth in vivo

Given that KRAS-interacting proteins could have either positive or negative effects on tumour growth, we first assessed whether we could detect gene-targeting events that have deleterious effects on tumour fitness using Tuba-seq. We initiated tumours in *Kras*<sup>L<sup>SL</sup>-G12D/+</sup>;*Rosa26*<sup>L<sup>SL</sup>-tdTomato</sup>;*H11*<sup>L<sup>SL</sup>-Cas9</sup> (*KT*;*H11*<sup>L<sup>SL</sup>-Cas9</sup>) and control *KT*

mice with a pool of barcoded Lenti-sgRNA/Cre vectors targeting two essential genes (*Pcna* and *Rps19*), a known tumour suppressor (*Apc*)<sup>20,29</sup>, and several inert sgRNAs (Lenti-sg*Essential*/Cre; Extended Data Fig. 2a). After 12 weeks of tumour growth, we performed Tuba-seq on bulk tumour-bearing lungs (Extended Data Fig. 2b). By incorporating measures of tumour number and size, we could confidently identify genetic deficiencies that reduced tumour fitness (Extended Data Fig. 2c–g and Methods).

To quantify the impact of inactivating our panel of KRAS-interacting proteins on oncogenic KRAS<sup>G12D</sup>-driven lung tumour growth in vivo, we generated a pool of barcoded Lenti-sgRNA/Cre vectors targeting the genes that encode these proteins, as well as sgInert controls and vectors targeting an essential gene (*Pcna*) and a known tumour suppressor (*Rb1*, Lenti-sg*KrasIP*/Cre; Fig. 1d). Given the importance of farnesylation in KRAS localization and signalling, sgRNA targeting of *Fnta* served as a control for KRAS dependency<sup>30,31</sup>. We initiated tumours with the Lenti-sg*KrasIP*/Cre pool in *KT*;*H11*<sup>L<sup>SL</sup>-Cas9</sup> and *KT* mice and calculated metrics of tumour size and number after 12 weeks of tumour growth (Fig. 1e). To our surprise, inactivation of the *Kras* paralogues *Hras* and *Nras* resulted in the most dramatic increases in tumour growth. Inactivation of *Cand1* also increased tumour size, while inactivation of several genes including *Fnta*, *Nme2*, *Rap1gds1* and *Aldh1a* decreased tumour size and/or number, suggesting reduced cancer cell fitness (Fig. 1f and Supplementary Fig. 3a–d).

Given the fundamental importance of the p53 tumour suppressor in oncogenic KRAS-driven lung cancer, as well as previous data suggesting crosstalk between RAS and p53 signalling<sup>19,32,33</sup>, we determined whether p53 deficiency changed the impact of inactivating KRAS-interacting proteins on tumour growth. We initiated tumours with the Lenti-sg*KrasIP*/Cre pool in *Kras*<sup>L<sup>SL</sup>-G12D/+</sup>;*Rosa26*<sup>L<sup>SL</sup>-tdTom</sup>;*p53*<sup>flx/flx</sup>;*H11*<sup>L<sup>SL</sup>-tdTom</sup> (*KT*;*p53*<sup>flx/flx</sup>;*H11*<sup>L<sup>SL</sup>-Cas9</sup>) mice and performed Tuba-seq after 12 weeks of tumour growth (Fig. 1e). The effects of inactivating each gene encoding a KRAS-interacting protein were generally consistent between the p53-proficient and p53-deficient settings (Fig. 1g and Extended Data Fig. 3e–h). Notably, inactivation of either *Hras* or *Nras* significantly increased the growth of p53-deficient tumours (Fig. 1g and Extended Data Fig. 3e). Collectively, these results suggest that HRAS and NRAS are tumour suppressors within in vivo models of oncogenic KRAS-driven lung cancer, while several other KRAS-interacting proteins have less consistent effects on tumour growth between p53-proficient and p53-deficient backgrounds (Extended Data Fig. 3e–h).

### Validation of HRAS and NRAS as tumour suppressors

To further validate the effect of inactivating six top candidate genes (*Hras*, *Nras*, *Cand1*, *Aldh1a*, *Fnta* and *Nme2*) on oncogenic KRAS-driven tumour growth in vivo and confirm that these results are driven by on-target effects, we generated three barcoded Lenti-sgRNA/Cre vectors targeting each gene. To contextualize the effects of inactivating these genes we also included vectors targeting three established tumour suppressors (*Lkb1*, *Rbm10* and *Rb1*) in this pool (Lenti-sg*Validation*/Cre; Fig. 2a)<sup>18,20,34</sup>. We initiated tumours with the Lenti-sg*Validation*/Cre pool in *KT*;*H11*<sup>L<sup>SL</sup>-Cas9</sup> and *KT* mice and assessed metrics of tumour initiation and growth 12 weeks after tumour initiation (Fig. 2b,c). Targeting *Fnta* consistently reduced growth across all three sgRNAs, while the impact of inactivating *Aldh1a* and *Nme2* was more variable (Fig. 2d and Extended Data Fig. 4). Most importantly, all sgRNAs targeting *Hras* and *Nras* significantly increased tumour growth (Fig. 2d,e and Extended Data Fig. 4b). Notably, *Hras* inactivation increased tumour growth to a similar extent as inactivation of the *Rb1* and *Rbm10* tumour suppressors (Fig. 2d and Extended Data Fig. 4b). These results suggest a potentially pivotal role for wild-type HRAS and NRAS in suppressing oncogenic KRAS-driven lung tumour growth in vivo.

We also validated the tumour-suppressive functions of HRAS and NRAS by initiating tumours in *KT*;*H11*<sup>L<sup>SL</sup>-Cas9</sup> mice with individual sgInert-, sgHras- or sgNras-containing Lenti-sgRNA/Cre vectors



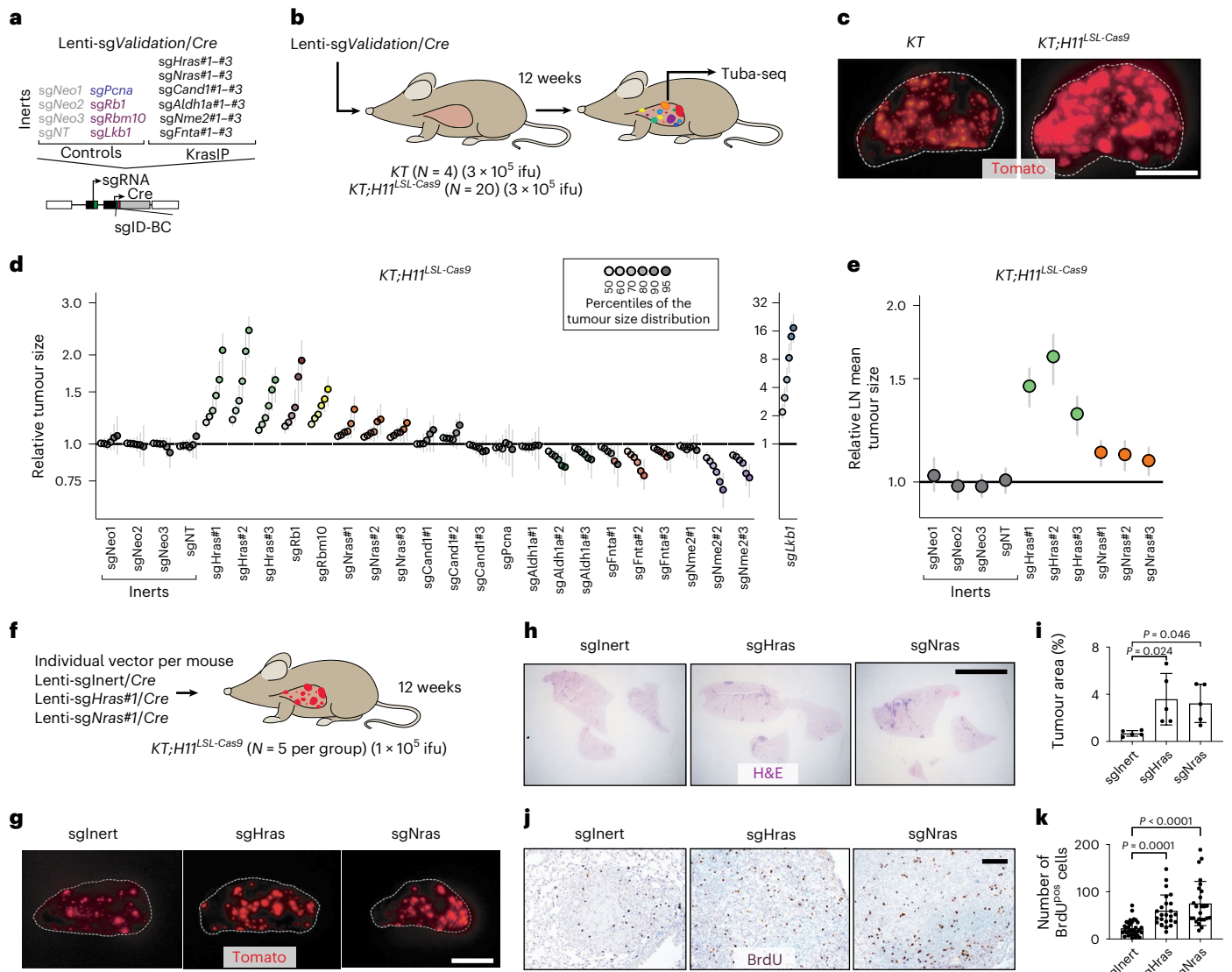


**Fig. 2 | HRAS and NRAS are potent suppressors of KRAS<sup>G12D</sup>-driven lung cancer growth in vivo.** **a**, Lenti-sgValidation/Cre targets candidate mediators of KRAS-driven lung tumour growth (three sgRNAs per gene). **b**, Tumours were initiated in *KT* and *KT;H11<sup>LSL-Cas9</sup>* mice through intratracheal delivery of Lenti-sgValidation/Cre, and Tuba-seq was performed on each tumour-bearing lung. **c**, Fluorescence images of lung lobes 12 weeks after tumour initiation. Representative of five *KT* and 15 *KT;H11<sup>LSL-Cas9</sup>* mice. Scale bar, 5 mm. Lung lobes are outlined with a white dashed line. **d**, Points denote tumour sizes at indicated percentiles for each sgRNA relative to the size of sgInert-containing tumours at the corresponding percentiles in *KT;H11<sup>LSL-Cas9</sup>* mice. Genes are ordered by 95th percentile tumour size, with sgInerts on the left. Note that *sgLkb1* is plotted on a separate scale to facilitate visualization. The line at  $y = 1$  indicates no effect relative to sgInert. Percentiles that are significantly different from sgInert (two-sided FDR-adjusted  $P < 0.05$ ) are in colour. **e**, Targeting *Hras* or *Nras* significantly increases mean tumour size relative to sgInerts, assuming a log-normal distribution of tumour sizes (LN mean). For **d** and **e**, error bars indicate 95%

confidence intervals around the point estimate of the test statistic. Confidence intervals and  $P$  values were calculated using nested bootstrap resampling across 20 *KT;H11<sup>LSL-Cas9</sup>* mice. **f**, Schematic of tumour initiation with individual Lenti-sgRNA/Cre vectors. **g**, Fluorescence images of lungs from *KT;H11<sup>LSL-Cas9</sup>* mice 12 weeks after tumour initiation with Lenti-sgRNA/Cre vectors. Representative of five mice per group. Scale bar, 5 mm. **h**, Representative H&E images of lungs from *KT;H11<sup>LSL-Cas9</sup>* mice after tumour initiation with Lenti-sgRNA/Cre vectors. Scale bar, 5 mm. **i**, Tumour burden in *KT;H11<sup>LSL-Cas9</sup>* mice with tumours initiated with Lenti-sgRNA/Cre vectors. Error bars are mean  $\pm$  s.d.. Each dot represents relative tumour area (percentage of total lung area) from one mouse.  $N = 5$  animals (one-way ANOVA). **j**, Representative BrdU staining images of lungs from *KT;H11<sup>LSL-Cas9</sup>* mice after tumour initiation with Lenti-sgRNA/Cre vectors. Scale bar, 100  $\mu$ m. **k**, Quantification of proliferating cells in *KT;H11<sup>LSL-Cas9</sup>* mice with tumours initiated with Lenti-sgRNA/Cre vectors. Error bars are mean  $\pm$  s.d. Each dot is a tumour (sgNeo:  $N = 34$ , sgHras:  $N = 24$ , sgNras:  $N = 25$ ).  $N = 5$  animals (one-way ANOVA).

genes can function as tumour suppressors in certain contexts (Extended Data Fig. 5b,c)<sup>10,15</sup>. To further assess the functions of HRAS and NRAS in oncogenic KRAS-driven human adenocarcinoma cell lines, we performed gain- and loss-of-function studies on H23 (KRAS<sup>G12C</sup>) and H727 (KRAS<sup>G12V</sup>) cells under growth-factor-restricted growth conditions. We inactivated *HRAS* and *NRAS* using CRISPR/Cas9 and generated variants with doxycycline-inducible wild-type *HRAS* re-expression (Extended

Data Fig. 5d). Inactivation of *HRAS* or *NRAS* in oncogenic KRAS-driven cells increased proliferation when cells were grown with limited serum and increased clonal growth potential in anchorage-independent conditions (Fig. 3a,c,d). Re-expression of HRAS in these *HRAS*-null cells impaired proliferation and clonal growth (Fig. 3b,e,f and Extended Data Fig. 5e). H23 cells with inactivated *HRAS* or *NRAS* also formed larger and more proliferative tumours after intravenous and subcutaneous

transplantation (Fig. 3g–k and Extended Data Fig. 5f–i). These results demonstrate that wild-type HRAS and NRAS can suppress the growth of oncogenic KRAS-driven human lung cancer cells in vitro and in vivo, further suggesting that HRAS and NRAS are tumour suppressors in oncogenic KRAS-driven lung adenocarcinoma.

### RAS paralogue inactivation increases signalling downstream of oncogenic KRAS

Wild-type KRAS has been shown to be tumour-suppressive in multiple experimental models of oncogenic KRAS-driven cancer, probably due to its ability to interact and compete with oncogenic KRAS<sup>G12D</sup><sup>36–38</sup>. We have demonstrated that wild-type HRAS and NRAS suppress oncogenic KRAS<sup>G12D</sup>-driven lung cancer growth in vivo. We first assessed the expression of KRAS, HRAS and NRAS in human and mouse lung cancer cells. HRAS and NRAS are more highly expressed than KRAS in KRAS-driven lung cancer cells, supporting their roles in regulating KRAS signalling (Extended Data Fig. 6a,b). To further explore the molecular mechanism driving this effect, we assessed whether HRAS and NRAS alter signalling downstream of oncogenic KRAS. We performed pERK immunohistochemistry on lung tumours initiated with Lenti-sgRNA/Cre vectors containing sgInert, sgHras or sgNras in *KT;HII<sup>LSL-Cas9</sup>* mice. Inactivation of *HRAS* or *NRAS* increased the number of pERK-positive cells in KRAS<sup>G12D</sup>-driven lung cancer (Fig. 4a and Extended Data Fig. 6c). Subcutaneous tumours from H23 cells with inactivated *HRAS* or *NRAS* also contained more pERK-positive cells compared with tumours from wild-type (sgSAFE) H23 cells (Fig. 4b and Extended Data Fig. 6d). Finally, sorted cancer cells from *KT;HII<sup>LSL-Cas9</sup>* mice with lung tumours initiated with Lenti-sgHras/Cre also had greater pERK and pAKT compared with those from tumours initiated with Lenti-sgInert/Cre (Fig. 4c).

Inactivation of either *Hras* or *Nras* in mouse (HC494) and human (H23 and HOP62) oncogenic KRAS-driven cell lines increased ERK phosphorylation, while their effects on AKT phosphorylation were more cell context dependent (Fig. 4d,e). Re-expression of wild-type HRAS in HRAS-null H23 and HOP62 human lung cancer cells reduced ERK phosphorylation while again having a cell-context-dependent effect on AKT phosphorylation (Fig. 4f and Extended Data Fig. 6e). Furthermore, re-expression of either HRAS or NRAS in *HRAS/NRAS* double-knockout HOP62 cells reduced pERK. Previous publications have shown that inactivating wild-type *KRAS* increases sensitivity to MEK inhibitors<sup>37,39</sup>. Consistent with these studies, inactivation of *HRAS* in H23 cells modestly increased sensitivity to the MEK inhibitor trametinib while re-expression of HRAS made cells more resistant (Fig. 4g,h). These data suggest that inactivation of *HRAS* or *NRAS* hyper-activates MAPK-ERK signalling in KRAS mutant cancer cells<sup>40–42</sup>.

### RAS paralogues suppress oncogenic KRAS–KRAS interaction

RAS proteins interact and form functional clusters on membranes to efficiently recruit downstream effectors<sup>43–45</sup>. Whether RAS proteins form dimers or oligomers through direct interactions or through close physical proximity is debated within the field<sup>16,46,47</sup>. We assessed whether HRAS and NRAS interact with KRAS. Both AP/MS data and co-immunoprecipitation experiments suggest that HRAS and NRAS interact with KRAS<sup>G12D</sup>, supporting the existence of heterotypic RAS–RAS interactions, possibly through a domain containing the  $\alpha 4/\alpha 5$  interface (Fig. 5a and Extended Data Fig. 7a,b). To assess the ability of RAS paralogues to interact with oncogenic KRAS<sup>G12D</sup>, we adapted a split-luciferase reporter system, which relies on luciferase complementation to quantify RAS–RAS interactions in living cells (Fig. 5b)<sup>16</sup>. We first used this split-luciferase reporter system to confirm the interaction between HRAS and NRAS with KRAS<sup>G12D</sup> (Extended Data Fig. 7c–e)<sup>16</sup>. Through expression of wild-type KRAS, HRAS or NRAS in KRAS<sup>G12D</sup>–KRAS<sup>G12D</sup> interaction reporter cells and control reporter cells, we found that all wild-type RAS paralogues can disrupt KRAS<sup>G12D</sup>–KRAS<sup>G12D</sup> interactions. While the other RAS family members RAC1 or RALA did not impact KRAS<sup>G12D</sup>–KRAS<sup>G12D</sup> interactions,

we validated the RAPIA–KRAS<sup>G12D</sup> interaction that was predicted from the initial AP/MS data (Fig. 5c and Extended Data Fig. 7f–i). Lastly, we overexpressed HRAS in KRAS<sup>G12D</sup>-expressing 293T cells and found HRAS–KRAS<sup>G12D</sup> interaction reduced BRAF–KRAS<sup>G12D</sup> interactions (Extended Data Fig. 7j).

### Patient-derived HRAS and NRAS mutations impair interaction with oncogenic KRAS

Our findings suggest that the tumour-suppressive function of wild-type HRAS and NRAS are mediated, at least in part by competitive interactions with oncogenic KRAS. We therefore hypothesized that there could be *HRAS* and *NRAS* mutations in human tumours with oncogenic *KRAS* that impair this interaction. To evaluate this possibility, we analysed data from AACR Project GENIE<sup>48</sup>. Mutations in *HRAS* and *NRAS* were rare (pan-cancer frequency of non-synonymous mutations was 0.83% and 2.87%, respectively). The majority of these were oncogenic mutations in codons 12, 13 or 61 that occurred in samples lacking oncogenic *KRAS* (Extended Data Fig. 8a,b). We did, however, identify multiple rare non-oncogenic *HRAS* and *NRAS* mutations (Fig. 5d and Extended Data Fig. 8c,d). We next assessed the ability of these mutants to interact with oncogenic KRAS. We measured the ability of four HRAS mutants and five NRAS mutants, as well as a control Y64A HRAS mutant that has been suggested to reduce HRAS–HRAS dimerization<sup>47</sup>, to inhibit KRAS<sup>G12D</sup>–KRAS<sup>G12D</sup> interactions. This identified two HRAS mutants (T50M and R123C) and one NRAS mutant (R102Q) that are unable to reduce KRAS<sup>G12D</sup>–KRAS<sup>G12D</sup> interactions (Fig. 5e and Supplementary Fig. 8e,f). Interestingly, both HRAS<sup>T50</sup> and HRAS<sup>R123</sup> are located close to the predicted HRAS–KRAS<sup>G12D</sup> interface involving the  $\alpha 4$  and  $\alpha 5$  helices (Fig. 5f and Extended Data Fig. 9). These findings are consistent with a model in which interaction of wild-type RAS paralogues with oncogenic KRAS suppresses tumour growth, such that mutations that impair this interaction are beneficial to tumour growth.

Previous publications have shown that RAS proteins differentially bind to RAS effectors and thus could function differently in their downstream signalling<sup>10,49</sup>. Re-analysis of HRAS and NRAS AP/MS datasets shows that the binding affinity of GTP-bound HRAS to RAF is more similar to GDP-bound KRAS than to its activated, GTP-bound form, suggesting that RAS heterodimers containing HRAS may be less able to activate downstream oncogenic signalling (Fig. 5g)<sup>10</sup>. To test this hypothesis, we re-expressed wild-type HRAS, HRAS<sup>Y64A</sup> or the two patient-derived HRAS<sup>T50M</sup> and HRAS<sup>R123C</sup> mutants in *HRAS*-null lung cancer cells. Re-expression of wild-type HRAS, but not any of the three mutants, reduced ERK phosphorylation and cell proliferation (Fig. 5h,i). Similarly, re-expression of wild-type NRAS, but not NRAS<sup>R102Q</sup>, suppressed ERK phosphorylation and proliferation in *NRAS*-null lung cancer cells (Extended Data Fig. 8g,h). These results further suggest that RAS paralogue imbalance alters oncogenic KRAS signalling via oncogenic KRAS–wild-type RAS paralogue interactions and is thus a driver of lung cancer growth.

### HRAS and NRAS are specific suppressors of oncogenic KRAS-driven lung cancer growth

Our in vivo data demonstrate that HRAS and NRAS function as tumour suppressors, and our in vitro results suggest that these suppressive effects are mediated through the interaction of these RAS paralogues with oncogenic KRAS. If the mechanism by which HRAS and NRAS suppress tumour growth is mediated by interactions with oncogenic KRAS, then these proteins should not be tumour suppressors in lung adenocarcinomas in which activation of the RAS/RAF/MEK signalling pathway occurs downstream of KRAS. To test this directly in autochthonous tumours, we initiated tumours in mouse models of oncogenic KRAS-driven and oncogenic BRAF-driven lung cancer using a subpool of barcoded Lenti-sgRNA/Cre vectors (Lenti-sgMultiGEMM/Cre; Fig. 6a). In addition to vectors targeting *Hras* and *Nras*, this pool contained vectors targeting several known tumour suppressors (*Apc*, *Rbm10*

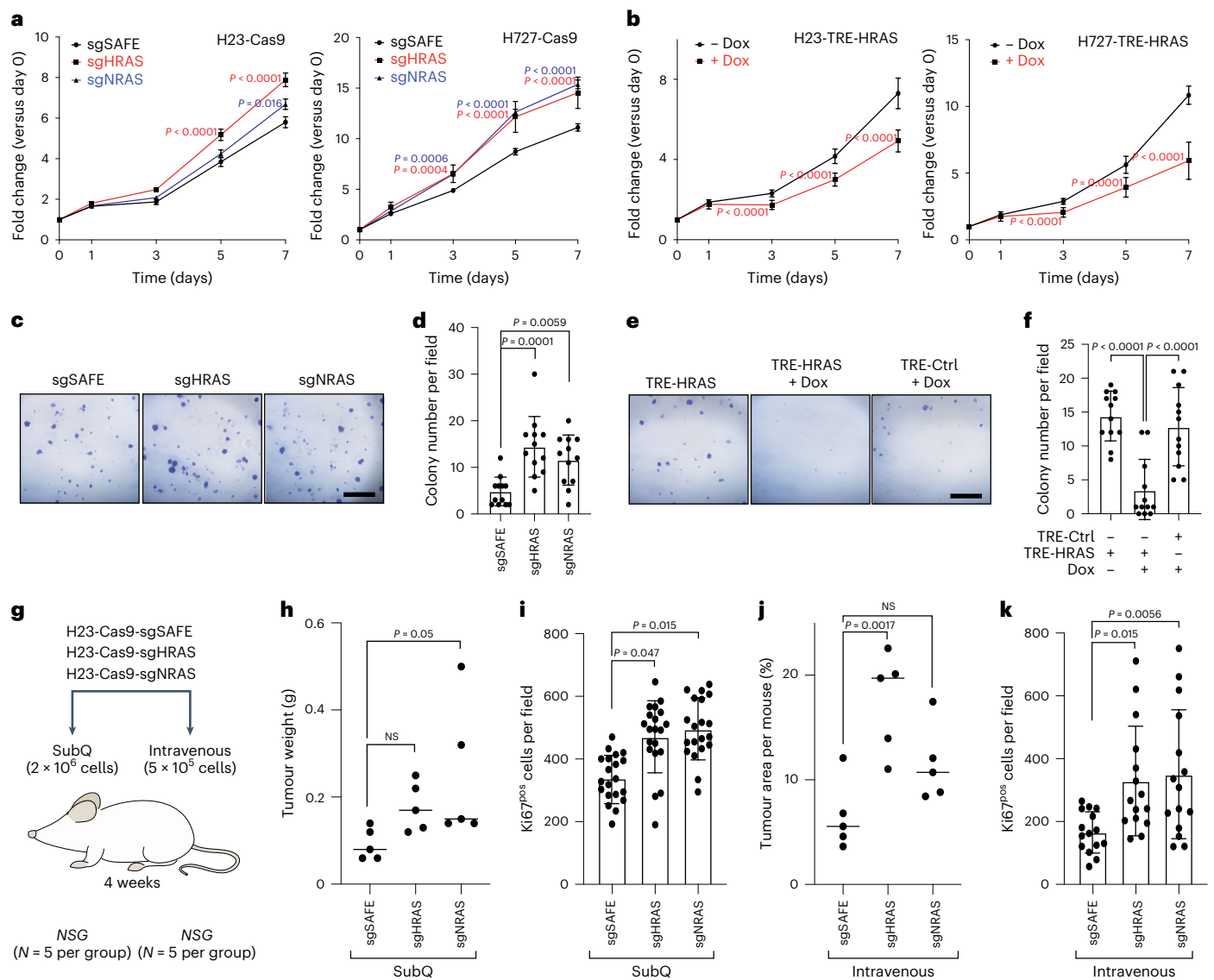


**Fig. 3 | Wild-type HRAS and NRAS constrain the growth of human KRAS-driven cancer cell lines.** **a**, Wild-type (sgSAFE) or *HRAS*- or *NRAS*-knockout cells were seeded in 96-well plates and cultured under limited serum (1%). Cell numbers were measured via CCK8 assay. Points are mean  $\pm$  s.d. of 12 wells normalized to day 0 (one-way ANOVA). **b**, Re-expression of wild-type HRAS suppresses proliferation of *HRAS*-null H23 and H727 cells. TRE-*HRAS* cells were seeded in 96-well plates and cultured under limited serum (1%) with or without 50 ng ml<sup>-1</sup> doxycycline (Dox) and cell numbers were measured via CCK8 assay. Points are mean  $\pm$  s.d. of eight wells normalized to day 0 (one-tailed *t*-test). **c, d**, Inactivation of *HRAS* or *NRAS* increases H23 colony formation. Wild-type (sgSAFE), *HRAS*-knockout (sgHRAS) or *NRAS*-knockout (sgNRAS) H23 cells were seeded at 1,000 cells per well in six-well plates and grown for 2 weeks. Cells were stained with crystal violet. **c**, Representative images. Scale bar, 5 mm. **d**, Mean  $\pm$  s.d. of colony number from 12 fields (one-way ANOVA). **e, f**, Re-expression of wild-type HRAS suppresses *HRAS*-null H23 cell colony formation.

Cells were seeded at 1,000 cells per well in six-well plates and grown with or without 50 ng ml<sup>-1</sup> Dox for 2 weeks. Cells were stained with crystal violet. **e**, Representative images. Scale bar, 5 mm. **f**, Mean  $\pm$  s.d. of colony number from 12 fields (one-way ANOVA). **g–k**, Inactivation of wild-type *HRAS* or *NRAS* increases H23 cell growth after transplantation. **g**, Schematic of tumour initiation by transplantation of H23 cells with inactivation of *HRAS* or *NRAS* in NSG mice. **h**, Tumour weight from subcutaneous (SubQ) transplantation of indicated cells, with each dot representing a mouse and values presented as mean. **i**, Ki67<sup>pos</sup> cell number in tumour sections from SubQ transplantation of indicated cells, shown as mean  $\pm$  s.d. value of 20 fields. **j**, Tumour area (percentage of human mitochondria<sup>pos</sup> area) from intravenous transplantation of indicated cells, with each dot representing a tumour and values presented as mean. **k**, Ki67<sup>pos</sup> cell number in tumour sections from intravenous transplantation of indicated cells, shown as mean  $\pm$  s.d. value of 15 fields (200 $\times$ ). NS, not significant (one-way ANOVA).

and *Cdkn2a*) and other KRAS-interacting proteins (*Aldh1a* and *Nme2*), as well as control vectors (Fig. 6a). We initiated tumours with the Lenti-sgMultiGEMM/Cre pool in *KT* and *KT;H1<sup>LSL-Cas9</sup>* mice as well as in *Braf<sup>T</sup>;H1<sup>LSL-Cas9</sup>* mice that contain a Cre-regulated allele of oncogenic BRAF<sup>V618E</sup> (the mouse equivalent of human BRAF<sup>V600E</sup>) (Fig. 6b)<sup>50</sup>. Fifteen weeks after tumour initiation, the two models had similar maximum tumour sizes, but *Braf<sup>T</sup>;H1<sup>LSL-Cas9</sup>* mice had larger tumours of relatively uniform size, which is consistent with previous results (Fig. 6c–f)<sup>50</sup>.

Our Tuba-seq data also allowed us to compare the impact of the CRISPR/Cas9-inactivated genes across oncogenic contexts. Importantly, while inactivation of *Hras* or *Nras* increased the growth of oncogenic KRAS-driven lung tumours, inactivation of *Hras* or *Nras* had no effect on the growth of oncogenic BRAF-driven lung cancer (Fig. 6g and Extended Data Fig. 10). These results were consistent for both Lenti-sgRNA/Cre vectors targeting each gene. The known tumour suppressor genes assayed (*Apc*, *Cdkn2a* and *Rbm10*) generally retained their growth-suppressive

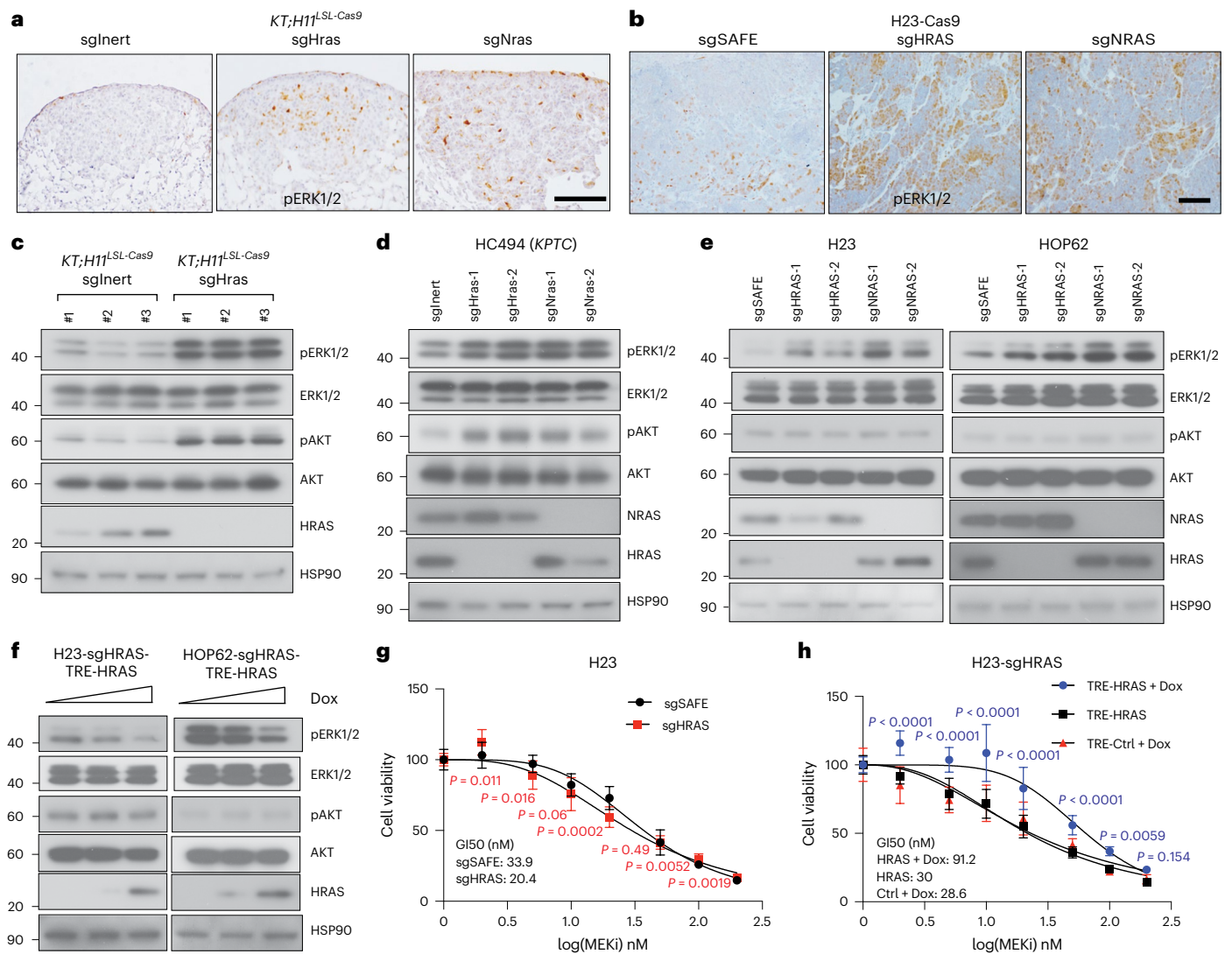


**Fig. 4 | Wild-type RAS paralogues suppress RAS signalling.** **a**, Images of pERK staining in *KT;H11<sup>LSL-Cas9</sup>* mice with tumours initiated with indicated Lenti-sgRNA/Cre vectors. Representative of >20 tumours across five mice per group. Scale bar, 100  $\mu$ m. **b**, Images of pERK staining in H23 cell subcutaneous tumours. Representative of >15 tumours across five mice per group. Scale bar, 100  $\mu$ m. **c**, Western blot of sorted cancer cells from *KT;H11<sup>LSL-Cas9</sup>* mice transduced with indicated Lenti-sgRNA/Cre vectors. **d**, Western blot of a murine lung adenocarcinoma cell line transduced with indicated Lenti-sgRNA vectors and selected with puromycin to generate stable knockout cell lines. Cells were cultured under limited serum (1%) for 2 days before protein extraction. **e**, Western blot of cultured human lung adenocarcinoma cell lines transduced with indicated Lenti-sgRNA vectors and selected with puromycin to generate stable knockout cell lines. Cells were cultured under limited serum (1%) for 2 days before protein extraction. **f**, Western blot of human lung adenocarcinoma cell lines re-expressing HRAS (TRE-HRAS) under doxycycline (Dox) treatment.

HRAS-null cells were re-transduced with lentiviral vector expressing TRE-HRAS to generate stable HRAS re-expressing cells (sgHRAS-TRE-HRAS). To re-express HRAS, cells were treated with 0, 1 or 2 ng ml<sup>-1</sup> Dox and cultured under limited serum (1%) for 2 days before protein extraction. In **c–f**, HSP90 is a loading control. **g**, 50% cell growth inhibition concentration (GI50) values to the MEK inhibitor trametinib among wild-type and *HRAS*-null H23 cells treated with the indicated doses of trametinib for 4 days. Cell numbers were measured via CCK8 assay and normalized to cells treated with vehicle. Each data point is shown as mean  $\pm$  s.d. of 12 wells (one-tailed *t*-test). **h**, GI50 values to the MEK inhibitor trametinib among *HRAS*-null H23 cells (H23-sgHRAS) re-expressing HRAS in the presence (HRAS + Dox) or absence (HRAS) of doxycycline plus the indicated dose of trametinib for 4 days. Cell numbers were measured via CCK8 assay and normalized to cells treated with vehicle. Each data point is shown as mean  $\pm$  s.d. of 12 wells (one-way ANOVA).

effects in the BRAF-driven model, suggesting that the abrogation of effect observed for *Hras* and *Nras* is not due to a generic inability of additional alterations to increase BRAF-driven lung tumour growth (Fig. 6h and Extended Data Fig. 10). Thus, HRAS and NRAS specifically suppress oncogenic KRAS-driven tumour growth in vivo.

We also identified several other instances of oncogene-tumour suppressor epistasis. For instance, *Apc* inactivation has a greater effect on BRAF-driven lung cancer, whereas *Rbm10* inactivation has a greater effect on KRAS-driven lung cancer (Fig. 6h and Extended Data Fig. 10). In contrast, inactivation of *Nme2*, *Fnta* and *Aldh1a* reduced initiation

and growth of oncogenic KRAS-driven and oncogenic BRAF-driven lung cancer, suggesting that they are generally required for optimal lung cancer growth in vivo (Extended Data Fig. 10). Thus, our paired screens not only localized the effect of *Hras* and *Nras* inactivation, but also highlighted the value of this approach in uncovering alterations that have effects within or across oncogenic contexts.

## Discussion

Oncogenic KRAS-driven lung cancer is a leading cause of cancer-related deaths. Despite the identification of oncogenic RAS almost half a

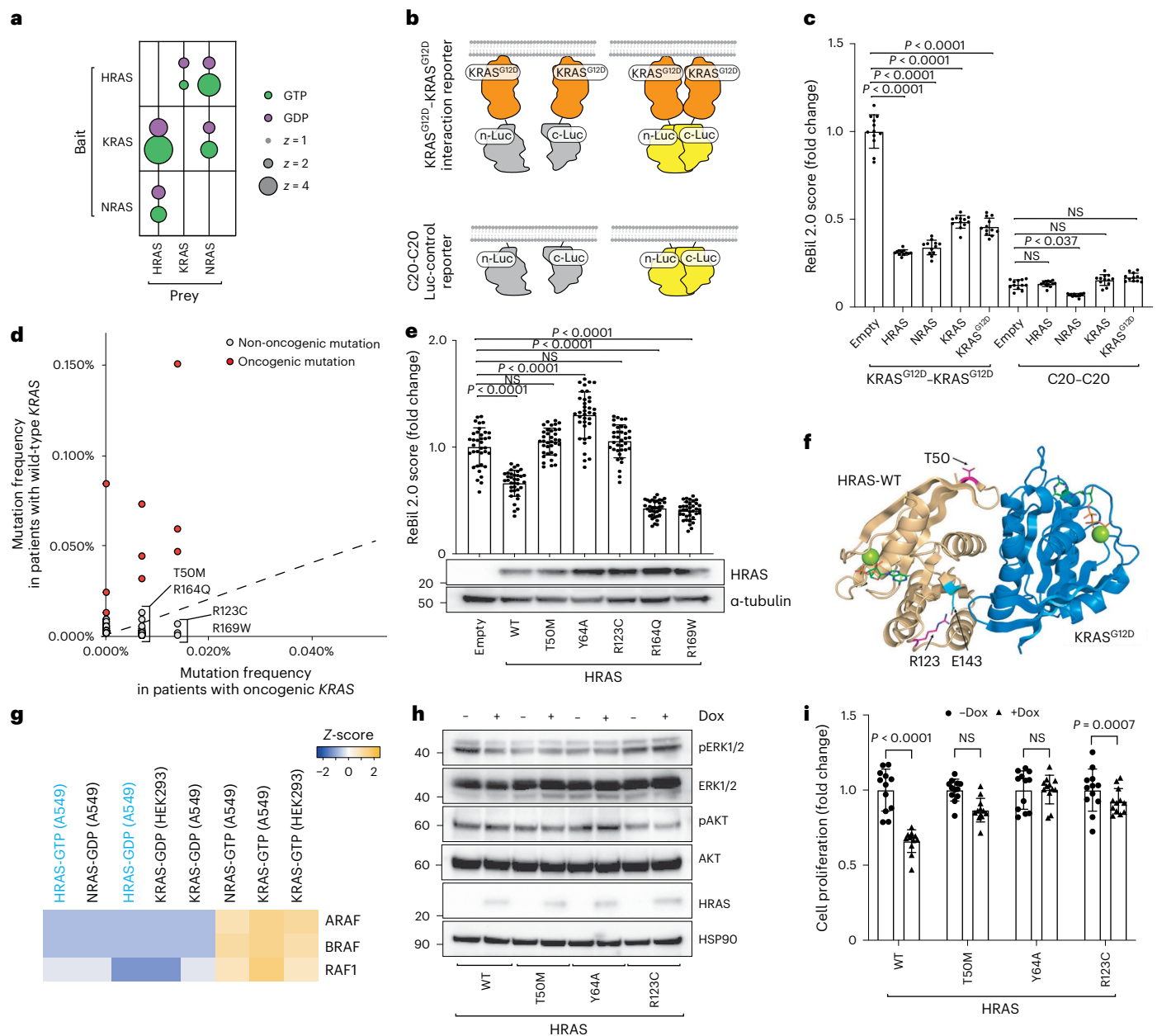


**Fig. 5 | Wild-type RAS paralogues fine-tune RAS signalling through interaction with oncogenic KRAS.** **a**, Enrichment of RAS paralogues in AP/MS experiments with HRAS, KRAS and NRAS as baits. **b**, Diagram of the ReBiL2.0 split luciferase system. KRAS<sup>G12D</sup>-KRAS<sup>G12D</sup> interactions were quantified by normalized luminescent signal generated by membrane-association-facilitated interactions of split-luciferase fused to the N-terminus of KRAS<sup>G12D</sup> (upper). Split-luciferase fused to the last 20 amino acids of KRAS (C20) is used as a control for background split-luciferase interactions (lower). **c**, 293T cells expressing nLuc-KRAS<sup>G12D</sup>/cluc-KRAS<sup>G12D</sup> or nLuc-C20/cluc-C20 with or without exogenous KRAS, HRAS or NRAS were cultured in limited serum (1%) for 24 h. Points are mean  $\pm$  s.d. ReBiL2.0 score of 12 wells normalized to cells transduced with empty vector. NS, not significant (one-way ANOVA). **d**, Pan-cancer frequency of HRAS mutations in wild-type and oncogenic KRAS-driven tumours. The dashed line indicates equal mutation frequency. Four mutations chosen for further validation in this study are highlighted. **e**, U2OS-764 (nLuc-KRAS<sup>G12D</sup>/cluc-KRAS<sup>G12D</sup>) cells expressing wild-type or mutant HRAS were cultured in limited serum (1%) with 100 ng ml<sup>-1</sup>

Dox for 24 h. Points are mean  $\pm$  s.d. ReBiL2.0 score of 36 wells normalized to cells transduced with empty vector. HRAS protein expression level in corresponding cells is shown by western blot. NS, not significant (one-way ANOVA). **f**, HRAS<sup>T50M</sup> and HRAS<sup>R123C</sup> are located close to the predicted HRAS-KRAS interaction interface. Residue R123 (magenta) makes an intrachain salt bridge with E143 (cyan). **g**, Prey RAF proteins enriched in each experiment with the indicated baits in A549 cells or HEK293 cells. **h**, Western blot of cultured HRAS-null HOP62 cells (HOP62-Cas9-sgHRAS) re-expressing wild-type or mutant HRAS under Dox treatment. Cells were cultured under limited serum (1%) for 2 days before protein extraction. **i**, Proliferation of cultured HRAS-null HOP62 cells (HOP62-Cas9-sgHRAS) re-expressing wild-type or mutant HRAS under Dox treatment. Cells were cultured in limited serum (1%) with or without Dox for 4 days. Cell viability was measured via CCK8 assay and normalized to cells treated with vehicle. Re-expression of HRAS mutants had no effect on cell proliferation. Points are mean  $\pm$  s.d. of 12 wells. NS, not significant (one-tailed *t*-test).

century ago, the function of many RAS-interacting proteins remains largely unknown. KRAS and other RAS family proteins have been reported to form dimers and nanoclusters<sup>16,46,47</sup>. Importantly, both

in vitro and in vivo studies suggest that KRAS-KRAS interactions influence effector protein activation, cellular transformation and tumour growth<sup>45</sup>. Multiple lines of evidence, including observation of loss of

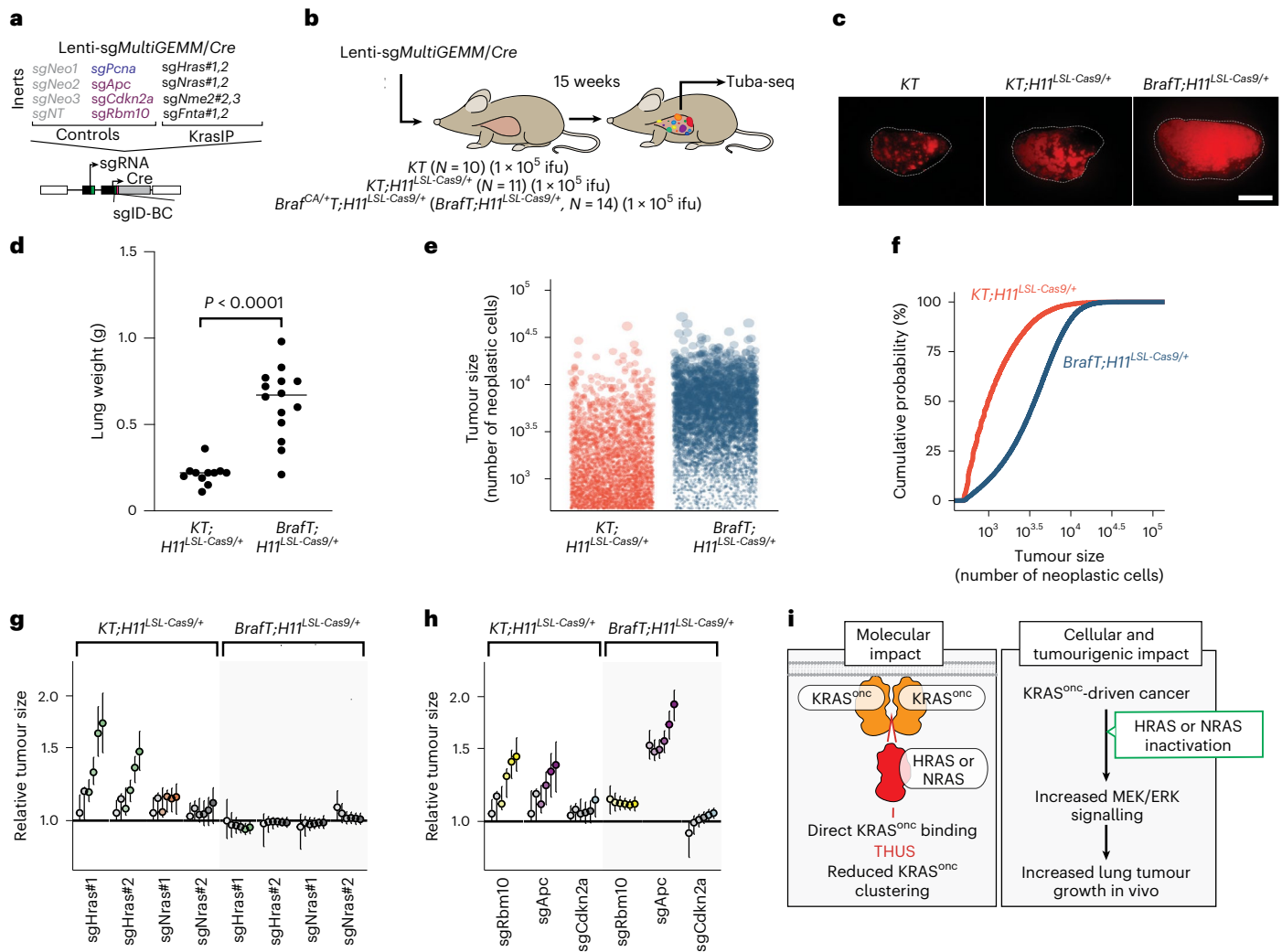


**Fig. 6 | Paired screens in KRAS-driven and BRAF-driven lung cancer models validate HRAS and NRAS as KRAS-specific tumour suppressors.** **a, b,** Schematic of pairwise screens to assess tumour-suppressive function in KRAS- and BRAF-driven lung cancer. Tumours were initiated in *KT;H11<sup>LSL-Cas9/+</sup>* and *Braf<sup>CA/+</sup>;H11<sup>LSL-Cas9/+</sup>* (*BrafT;H11<sup>LSL-Cas9/+</sup>*) mice through intratracheal delivery of Lenti-sgMultiGEMM/Cre, and Tuba-seq was performed on each tumour-bearing lung 15 weeks after initiation. **c,** Fluorescence images of representative lung lobes 15 weeks after tumour initiation. Scale bar, 5 mm. Lung lobes are outlined. **d,** Lung weights in *KT;H11<sup>LSL-Cas9/+</sup>* and *BrafT;H11<sup>LSL-Cas9/+</sup>* mice 15 weeks after tumour initiation. Each dot is a mouse, and mean values are indicated (one-tailed *t*-test). **e, f,** Size distribution of sgInert tumours in *KT;H11<sup>LSL-Cas9/+</sup>* and *BrafT;H11<sup>LSL-Cas9/+</sup>* mice. In **e**, each dot represents a tumour and has an area proportional to its size. A random sample of 1,000 tumours from each of five representative *KT;H11<sup>LSL-Cas9/+</sup>* and *BrafT;H11<sup>LSL-Cas9/+</sup>* mice is plotted. In **f**, the empirical cumulative distribution function of tumour sizes (>500 cells) across all *KT;H11<sup>LSL-Cas9/+</sup>* and *BrafT;H11<sup>LSL-Cas9/+</sup>* mice is plotted. **g,** Inactivation of either *Hras* or *Nras* increases tumour size in

*KT;H11<sup>LSL-Cas9/+</sup>* but not *BrafT;H11<sup>LSL-Cas9/+</sup>* models. **h,** Comparison of the effects of inactivation of known tumour suppressors on tumour size in *KT;H11<sup>LSL-Cas9/+</sup>* and *BrafT;H11<sup>LSL-Cas9/+</sup>* models. In **g** and **h**, points denote tumour sizes at indicated percentiles for each sgRNA relative to the size of sgInert-containing tumours at the corresponding percentiles in *KT;H11<sup>LSL-Cas9/+</sup>* and *BrafT;H11<sup>LSL-Cas9/+</sup>* mice. Line at *y* = 1 indicates no effect relative to sgInert. Error bars indicate 95% confidence intervals around the point estimate of the test statistic. Percentiles that are significantly different from sgInert (two-sided FDR-adjusted *P* < 0.05) are in colour. Confidence intervals and *P* values were calculated using a nested bootstrap resampling approach across 11 *KT;H11<sup>LSL-Cas9/+</sup>* mice and 14 *BrafT;H11<sup>LSL-Cas9/+</sup>* mice. **i,** Schematic of the function of wild-type RAS paralogues as tumour suppressors in oncogenic KRAS-driven lung cancer. Left: wild-type RAS paralogues competitively interact with oncogenic KRAS and suppress oncogenic KRAS clustering. Right: inactivation of wild-type RAS alleles, or ‘RAS paralogue imbalance’, increases activation of oncogenic KRAS signalling and promotes lung cancer growth.

the wild-type *KRAS* allele and copy number gain of oncogenic *KRAS* in human tumours, as well as functional studies in mouse models, suggest that wild-type *KRAS* is tumour-suppressive (also called ‘RAS allelic imbalance’), although the exact role of wild-type *KRAS* in lung cancer is still debated<sup>3,38,41,51,52</sup>. Recent data suggest that interactions also occur among HRAS, NRAS and KRAS, thus raising the question of the roles of wild-type HRAS and NRAS in oncogenic KRAS-driven cancer<sup>10,11,16</sup>.

By integrating AP/MS data with multiplexed somatic cell CRISPR/Cas9 editing in autochthonous mouse models, we assess the functional

impact of inactivating a panel of genes encoding KRAS-interacting proteins including the RAS paralogues HRAS and NRAS on lung cancer in vivo. We show that wild-type HRAS and NRAS are potent KRAS-specific tumour suppressors that interact with oncogenic KRAS, disrupt KRAS–KRAS interactions and suppress downstream RAS/MAPK signalling. These results support a model in which heterotypic interactions between RAS paralogues suppress oncogenic KRAS-driven lung cancer growth such that changes in the ratio of wild-type RAS paralogues to oncogenic KRAS can drive tumour growth, a phenomenon we term ‘RAS paralogue imbalance’.

Interestingly, our data suggest that HRAS is a more potent suppressor of tumour growth than NRAS in mouse models of oncogenic KRAS-driven lung adenocarcinoma, while NRAS appears to have stronger effects on KRAS–KRAS dimerization and downstream signalling in human cells. Our data suggest that NRAS may be slightly more potent than HRAS at inhibiting oncogenic KRAS–KRAS interactions (Extended Data Fig. 8c–g) but that the protein expression of the RAS paralogues can vary among cell types and cancer types (Extended Data Fig. 7a,b). Thus, per-molecule ability to disrupt KRAS–KRAS interaction, preferential interactions with downstream effectors, and the stoichiometry of KRAS, HRAS and NRAS proteins probably integrate to drive the cellular and in vivo phenotypes.

The impact of RAS paralogue imbalance may extend beyond lung cancer and KRAS codon 12 mutations. Germline *HRAS* deletion increases the development of KRAS-driven pancreatic cancer, skin papillomas and carcinogen-induced KRAS<sup>G61</sup> lung cancer<sup>52–54</sup>. However, the impact of inactivating RAS paralogues in cancers with different driver oncogenes (for example, oncogenic EGFR-driven lung cancer) is likely to be different since RAS proteins also serve as important components in growth factor signalling pathways. Whether RAS paralogue heterodimerization also impacts signalling during normal development, homeostasis or other diseases states remains unknown. Collectively, these findings suggest that modulating RAS protein interactions, such as by skewing the stoichiometry of oncogenic to wild-type RAS or by forcing inter-paralogue competition, could lead to therapeutic strategies.

Given the complexity of RAS signalling, other non-mutually exclusive mechanisms by which RAS paralogues could reduce oncogenic KRAS-driven cancer growth should be considered. For example, it has been reported that upstream regulators, such as SOS1, could bridge the interaction between oncogenic and wild-type RAS<sup>55</sup>. GDP-bound wild-type HRAS and NRAS could also compete with oncogenic KRAS for upstream guanine nucleotide exchange factors and thus reduce RAS signalling<sup>56</sup>. Additionally, it is possible that HRAS and NRAS compete with oncogenic KRAS for downstream effectors. Whether HRAS and NRAS also function through these alternative routes, and how different mechanisms are integrated to execute their tumour-suppressive functions, will require additional investigation.

The National Cancer Institute ‘RAS Pathway V2.0’, contains more than 200 proteins known or suspected to be involved in RAS signalling. Characterizing the role of these proteins in tractable in vivo models of RAS-driven cancer remains a challenge. Our study outlines a technological avenue to study KRAS-specific signalling components in a multiplexed manner. By harnessing the power of Tuba-seq, we quantified the effects of more than a dozen putative RAS pathway genes on tumour growth simultaneously. Furthermore, by performing paired screens in oncogenic KRAS-driven and oncogenic BRAF-driven cancer models, we localized the growth-suppressive effects of these RAS paralogues. Our study demonstrates the feasibility of performing in vivo genetic interaction screens, and the power of such approaches to provide insight into the mechanisms of tumour suppression. Future studies of this type should enable a more quantitative understanding of the role of RAS pathway components in oncogenesis.

## Online content

Any methods, additional references, Nature Portfolio reporting summaries, source data, extended data, supplementary information, acknowledgements, peer review information; details of author contributions and competing interests; and statements of data and code availability are available at <https://doi.org/10.1038/s41556-022-01049-w>.

## References

- Karnoub, A. E. & Weinberg, R. A. Ras oncogenes: split personalities. *Nat. Rev. Mol. Cell Biol.* **9**, 517–531 (2008).
- Cox, A. D., Fesik, S. W., Kimmelman, A. C., Luo, J. & Der, C. J. Drugging the undruggable RAS: mission possible? *Nat. Rev. Drug Discov.* **13**, 828–851 (2014).
- Zhou, B., Der, C. J. & Cox, A. D. in *Seminars in Cell & Developmental Biology* Vol. 58, 60–69 (Elsevier, 2016).
- Wennerberg, K., Rossman, K. L. & Der, C. J. The Ras superfamily at a glance. *J. Cell Sci.* **118**, 843–846 (2005).
- Hobbs, G. A., Der, C. J. & Rossman, K. L. RAS isoforms and mutations in cancer at a glance. *J. Cell Sci.* **129**, 1287–1292 (2016).
- Stephen, A. G., Esposito, D., Bagni, R. K. & McCormick, F. Dragging Ras back in the ring. *Cancer Cell* **25**, 272–281 (2014).
- Brose, M. S. et al. BRAF and RAS mutations in human lung cancer and melanoma. *Cancer Res.* **62**, 6997–7000 (2002).
- Prior, I. A., Lewis, P. D. & Mattos, C. A comprehensive survey of Ras mutations in cancer. *Cancer Res.* **72**, 2457–2467 (2012).
- Papke, B. & Der, C. J. Drugging RAS: know the enemy. *Science* **355**, 1158–1163 (2017).
- Kelly, M. R. et al. Combined proteomic and genetic interaction mapping reveals new RAS effector pathways and susceptibilities. *Cancer Discov.* **10**, 1950–1967 (2020).
- Broyde, J. et al. Oncoprotein-specific molecular interaction maps (SigMaps) for cancer network analyses. *Nat. Biotechnol.* **39**, 215–224 (2021).
- Zhou, Y. & Hancock, J. F. Deciphering lipid codes: K-Ras as a paradigm. *Traffic* **19**, 157–165 (2018).
- Wittinghofer, A. & Pal, E. F. The structure of Ras protein: a model for a universal molecular switch. *Trends Biochem. Sci.* **16**, 382–387 (1991).
- Omerovic, J., Hammond, D. E., Clague, M. J. & Prior, I. A. Ras isoform abundance and signalling in human cancer cell lines. *Oncogene* **27**, 2754–2762 (2008).
- Han, K. et al. CRISPR screens in cancer spheroids identify 3D growth-specific vulnerabilities. *Nature* **580**, 136–141 (2020).
- Li, Y.-C. et al. Analysis of RAS protein interactions in living cells reveals a mechanism for pan-RAS depletion by membrane-targeted RAS binders. *Proc. Natl Acad. Sci. USA* **117**, 12121–12130 (2020).
- Hingorani, S. R. et al. Preinvasive and invasive ductal pancreatic cancer and its early detection in the mouse. *Cancer Cell* **4**, 437–450 (2003).
- Cai, H. et al. A functional taxonomy of tumor suppression in oncogenic KRAS-driven lung cancer. *Cancer Discov.* **11**, 1754–1773 (2021).
- Rogers, Z. N. et al. Mapping the in vivo fitness landscape of lung adenocarcinoma tumor suppression in mice. *Nat. Genet.* **50**, 483–486 (2018).
- Rogers, Z. N. et al. A quantitative and multiplexed approach to uncover the fitness landscape of tumor suppression in vivo. *Nat. Methods* **14**, 737–742 (2017).
- Chuang, C.-H. et al. Molecular definition of a metastatic lung cancer state reveals a targetable CD109–Janus kinase–Stat axis. *Nat. Med.* **23**, 291–300 (2017).
- Ruiz, S., Santos, E. & Bustelo, X. R. RasGRF2, a guanosine nucleotide exchange factor for Ras GTPases, participates in T-cell signaling responses. *Mol. Cell Biol.* **27**, 8127–8142 (2007).
- Brandt, A. C., Koehn, O. J. & Williams, C. L. SmgGDS: an emerging master regulator of prenylation and trafficking by small GTPases in the Ras and Rho families. *Front. Mol. Biosci.* **8**, 542 (2021).
- Rowell, C. A., Kowalczyk, J. J., Lewis, M. D. & Garcia, A. M. Direct demonstration of geranylgeranylation and farnesylation of Ki-Ras in vivo. *J. Biol. Chem.* **272**, 14093–14097 (1997).
- Zhang, F. L. et al. Characterization of Ha-ras, N-ras, Ki-Ras4A, and Ki-Ras4B as in vitro substrates for farnesyl protein transferase and geranylgeranyl protein transferase type I. *J. Biol. Chem.* **272**, 10232–10239 (1997).

26. Takaya, A. et al. R-Ras regulates exocytosis by Rgl2/Rlf-mediated activation of RalA on endosomes. *Mol. Biol. Cell* **18**, 1850–1860 (2007).
27. Marais, R., Light, Y., Paterson, H. & Marshall, C. Ras recruits Raf-1 to the plasma membrane for activation by tyrosine phosphorylation. *EMBO J.* **14**, 3136–3145 (1995).
28. Campbell, J. D. et al. Distinct patterns of somatic genome alterations in lung adenocarcinomas and squamous cell carcinomas. *Nat. Genet.* **48**, 607–616 (2016).
29. Sánchez-Rivera, F. J. et al. Rapid modelling of cooperating genetic events in cancer through somatic genome editing. *Nature* **516**, 428–431 (2014).
30. Kohl, N. E. et al. Selective inhibition of ras-dependent transformation by a farnesyltransferase inhibitor. *Science* **260**, 1934–1937 (1993).
31. Rowinsky, E. K., Windle, J. J. & Von Hoff, D. D. Ras protein farnesyltransferase: a strategic target for anticancer therapeutic development. *J. Clin. Oncol.* **17**, 3631–3652 (1999).
32. Collisson, E. et al. Comprehensive molecular profiling of lung adenocarcinoma: The Cancer Genome Atlas Research Network. *Nature* **511**, 543–550 (2014).
33. Feldser, D. M. et al. Stage-specific sensitivity to p53 restoration during lung cancer progression. *Nature* **468**, 572–575 (2010).
34. Murray, C. W. et al. An LKB1–SIK axis suppresses lung tumor growth and controls differentiation. *Cancer Discov.* **9**, 1590–1605 (2019).
35. Tsherniak, A. et al. Defining a cancer dependency map. *Cell* **170**, 564–576.e16 (2017).
36. Staffas, A., Karlsson, C., Persson, M., Palmqvist, L. & Bergo, M. Wild-type KRAS inhibits oncogenic KRAS-induced T-ALL in mice. *Leukemia* **29**, 1032–1040 (2015).
37. Ambrogio, C. et al. KRAS dimerization impacts MEK inhibitor sensitivity and oncogenic activity of mutant KRAS. *Cell* **172**, 857–868.e15 (2018).
38. Kong, G. et al. Loss of wild-type Kras promotes activation of all Ras isoforms in oncogenic Kras-induced leukemogenesis. *Leukemia* **30**, 1542–1551 (2016).
39. Burgess, M. R. et al. KRAS allelic imbalance enhances fitness and modulates MAP kinase dependence in cancer. *Cell* **168**, 817–829.e15 (2017).
40. Young, A., Lou, D. & McCormick, F. Oncogenic and wild-type Ras play divergent roles in the regulation of mitogen-activated protein kinase signaling. *Cancer Discov.* **3**, 112–123 (2013).
41. Grabocka, E. et al. Wild-type H- and N-Ras promote mutant K-Ras-driven tumorigenesis by modulating the DNA damage response. *Cancer Cell* **25**, 243–256 (2014).
42. Zhou, Y. et al. Signal integration by lipid-mediated spatial cross talk between Ras nanoclusters. *Mol. Cell. Biol.* **34**, 862–876 (2014).
43. Zhou, Y. & Hancock, J. F. Ras nanoclusters: versatile lipid-based signaling platforms. *Biochim. Biophys. Acta Mol. Cell Res.* **1853**, 841–849 (2015).
44. Henis, Y. I., Hancock, J. F. & Prior, I. A. Ras acylation, compartmentalization and signaling nanoclusters. *Mol. Membr. Biol.* **26**, 80–92 (2009).
45. Inouye, K., Mizutani, S., Koide, H. & Kaziro, Y. Formation of the Ras dimer is essential for Raf-1 activation. *J. Biol. Chem.* **275**, 3737–3740 (2000).
46. Muratcioglu, S. et al. GTP-dependent K-Ras dimerization. *Structure* **23**, 1325–1335 (2015).
47. Lin, W.-C. et al. H-Ras forms dimers on membrane surfaces via a protein–protein interface. *Proc. Natl Acad. Sci. USA* **111**, 2996–3001 (2014).
48. AACR Project Genie Consortium. AACR Project GENIE: powering precision medicine through an international consortium. *Cancer Discov.* **7**, 818–831 (2017).
49. Terrell, E. M. et al. Distinct Binding Preferences between Ras and Raf Family Members and the Impact on Oncogenic Ras Signaling. *Mol. Cell* **76**, 872–884.e5 (2019).
50. Dankort, D. et al. A new mouse model to explore the initiation, progression, and therapy of BRAFV600E-induced lung tumors. *Genes Dev.* **21**, 379–384 (2007).
51. Dietrich, P. et al. Neuroblastoma RAS viral oncogene homolog (NRAS) is a novel prognostic marker and contributes to sorafenib resistance in hepatocellular carcinoma. *Neoplasia* **21**, 257–268 (2019).
52. Weyandt, J. D. et al. Wild-type Hras suppresses the earliest stages of tumorigenesis in a genetically engineered mouse model of pancreatic cancer. *PLoS ONE* **10**, e0140253 (2015).
53. To, M. D., Rosario, R., Westcott, P. M., Banta, K. L. & Balmain, A. Interactions between wild-type and mutant Ras genes in lung and skin carcinogenesis. *Oncogene* **32**, 4028–4033 (2013).
54. Weyandt, J. D., Carney, J. M., Pavlisko, E. N., Xu, M. & Counter, C. M. Isoform-specific effects of wild-type Ras genes on carcinogen-induced lung tumorigenesis in mice. *PLoS ONE* **11**, e0167205 (2016).
55. Jeng, H.-H., Taylor, L. J. & Bar-Sagi, D. Sos-mediated cross-activation of wild-type Ras by oncogenic Ras is essential for tumorigenesis. *Nat. Commun.* **3**, 1168 (2012).
56. Miller, M. S. & Miller, L. D. RAS mutations and oncogenesis: not all RAS mutations are created equally. *Front. Genet.* **2**, 100 (2012).

**Publisher's note** Springer Nature remains neutral with regard to jurisdictional claims in published maps and institutional affiliations.

Springer Nature or its licensor (e.g. a society or other partner) holds exclusive rights to this article under a publishing agreement with the author(s) or other rightsholder(s); author self-archiving of the accepted manuscript version of this article is solely governed by the terms of such publishing agreement and applicable law.

© The Author(s), under exclusive licence to Springer Nature Limited 2023

<sup>1</sup>Department of Genetics, Stanford University School of Medicine, Stanford, CA, USA. <sup>2</sup>Department of Biology, Stanford University, Stanford, CA, USA. <sup>3</sup>Cancer Biology Program, Stanford University School of Medicine, Stanford, CA, USA. <sup>4</sup>Baxter Laboratories, Stanford University School of Medicine, Stanford, CA, USA. <sup>5</sup>Molecular Therapeutics Program, Institute for Cancer Research, Fox Chase Cancer Center, Philadelphia, PA, USA. <sup>6</sup>Molecular and Cell Biology and Genetics Program, Drexel University College of Medicine, Philadelphia, PA, USA. <sup>7</sup>Gene Expression Laboratory, The Salk Institute for Biological Studies, La Jolla, CA, USA. <sup>8</sup>The Chan Zuckerberg BioHub, San Francisco, CA, USA. <sup>9</sup>Department of Pathology, Stanford University School of Medicine, Stanford, CA, USA. <sup>10</sup>These authors contributed equally: Rui Tang, Emily G. Shuldiner. ✉ e-mail: [mwinslow@stanford.edu](mailto:mwinslow@stanford.edu)

## Methods

### Mouse research

The use of mice for the current study has been approved by the Institutional Animal Care and Use Committee at Stanford University, protocol number 26696. *Kras<sup>LSL-G12D/+</sup>* (RRID:IMSR\_JAX:008179), *R26<sup>LSL-tdTomato</sup>* (RRID:IMSR\_JAX:007909) and *H11<sup>LSL-Cas9</sup>* (RRID:IMSR\_JAX:027632) mice have been previously described. They were on a C57BL/6:129 mixed background for the experiments in Figs. 1, 2 and 4, and were on a C57BL/6 background for the experiments in Fig. 6. The B6.129P2(Cg)-Braf<sup>f<sup>tm1Mmcm</sup>/J</sup> (*BRAF<sup>CA/+</sup>*) mice were initially generated by Dankort et al. and obtained from the Jackson Laboratory (RRID:IMSR\_JAX:017837). We used balanced sex of animals with age ranging from 8 to 15 weeks at the time of tumour initiation. Mice were housed at Stanford SIM1 barrier facility under a 12 h–12 h light–dark cycle with dark hours between 18:30 and 6:30. Housing temperature at 68–73 °F under 40–60% humidity.

### Cells and reagents

NCI-H23 (CRL-5800), NCI-H727 (CRL-5815) and HEK293T (CRL-3216) were originally purchased from ATCC; HC494 (*KPT*), HC367 (*KPT*) and MT658 (*KPT*) lung adenocarcinoma cells were generated in the Winslow Lab; U2OS-134-764np (nLuc-KRAS<sup>G12D</sup> cluc-KRAS<sup>G12D</sup>; KRAS<sup>G12D</sup> was fused to the N-termini of split luciferase proteins) cells were generated in the Wahl lab by Dr Yao-Cheng Li (Salk Institute for Biological Studies). HC494, HC367 and MT658 cells were cultured in Dulbecco's modified Eagle medium (DMEM) containing 10% FBS, 100 units ml<sup>-1</sup> penicillin and 100 µg ml<sup>-1</sup> streptomycin. H23 and H727 cells were cultured in RPMI 1640 medium containing 10% FBS, 100 units ml<sup>-1</sup> penicillin and 100 µg ml<sup>-1</sup> streptomycin. U2OS cells were cultured in DMEM/F12 (Thermo Fisher; phenol-red free), 10% FBS and 10 µg ml<sup>-1</sup> ciprofloxacin. All cell lines were confirmed to be mycoplasma negative (MycoAlert Detection Kit, Lonza).

Trametinib was purchased from MedChemExpress (HY-10999); 5-bromo-2'-deoxyuridine (10280879001) and D-luciferin (L9504-5MG) were purchased from Sigma-Aldrich. All plasmids used in this study are listed in Supplementary Table 1 and are available from our laboratory (key plasmids will be donated to Addgene).

### Design, generation, barcoding and production of lentiviral vectors

sgRNA sequences targeting the putative tumour suppressor genes were designed using CRISPick (<https://portals.broadinstitute.org/gppx/crispick/public>). All sgRNA sequences are presented in Supplementary Table 2. Each desired sgRNA vector was modified from our previously published pI13-U6-sgRNA-Pgk-Cre vector via site-directed mutagenesis (New England Biolabs, E0554S). The generation of the barcode (BC) fragment containing the 8-nucleotide sgID sequence and 20-nucleotide degenerate BC, and subsequent ligation into the vectors, were performed as previously described<sup>18,19</sup>.

Lentiviral vectors were produced using polyethylenimine-based transfection of 293T cells with delta8.2 and VSV-G packaging plasmids in 150 mm cell culture plates. Sodium butyrate (Sigma-Aldrich, B5887) was added 8 h after transfection to achieve a final concentration of 20 mM. Medium was refreshed 24 h after transfection. Twenty millilitres of virus-containing supernatant was collected 36, 48 and 60 h after transfection. The three collections were then pooled and concentrated by ultracentrifugation (112,000 g for 1.5 h) and resuspended overnight in 100 µl PBS, then frozen at -80 °C and thawed and pooled at equal ratios immediately before delivery to mice.

### Tumour initiation

Tumours were initiated by intratracheal delivery of 60 µl of lentiviral vectors dissolved in PBS. For the initial experiments in Figs. 1 and 2, tumours were allowed to develop for 12 weeks after delivery of a lentiviral pool that contained 19 barcoded Lenti-sgRNA/Cre vectors

(Lenti-sg*KrasIP/Cre*). Tumours were initiated in *Kras<sup>LSL-G12D</sup>; R26<sup>LSL-tdTomato</sup>* (*KT*), *KT;H11<sup>LSL-Cas9</sup>*, and *KT;p53<sup>fl/fl</sup>;H11<sup>LSL-Cas9</sup>* mice with  $1.95 \times 10^5$  infectious units (ifu) per mouse.

For the validation experiments in Fig. 3, tumours were allowed to develop for 15 weeks after delivery of a lentiviral pool that contained 26 barcoded Lenti-sgRNA/Cre vectors (Lenti-sg*Validation/Cre*). Tumours were initiated in *Kras<sup>LSL-G12D</sup>; R26<sup>LSL-tdTomato</sup>* (*KT*) and *KT;H11<sup>LSL-Cas9</sup>* mice with  $3 \times 10^5$  ifu per mouse.

For the individual sgRNA tumour initiation experiments in Fig. 3, tumours were allowed to develop for 12 weeks after delivery of individual sgRNA-expressing lentiviral vectors targeting *Neo2*, *Hras* or *Nras*. Tumours were initiated in *KT;H11<sup>LSL-Cas9</sup>* mice with  $1 \times 10^5$  ifu per mouse.

For the paired screen experiments in Fig. 6, tumours were allowed to develop for 15 weeks after delivery of a lentiviral pool that contained 15 barcoded Lenti-sgRNA/Cre vectors (Lenti-sg*MultiGEMM/Cre*). Tumours were initiated in *KT;H11<sup>LSL-Cas9/+</sup>* and *Braf<sup>P600E</sup>;R26<sup>LSL-tdTomato</sup>;H11<sup>LSL-Cas9/+</sup>* mice with  $3 \times 10^5$  ifu per mouse. Note that *KT;H11<sup>LSL-Cas9/+</sup>* rather than *KT;H11<sup>LSL-Cas9/LSL-Cas9</sup>* mice were used in this experiment to match the Cas9 dosage of the *BrafT;H11<sup>LSL-Cas9/+</sup>* mice, whereas *KT;H11<sup>LSL-Cas9/LSL-Cas9</sup>* mice were used in all other experiments. To evaluate the effects of Cas9 dosage on the tumour-suppressive effects of the Lenti-sg*MultiGEMM/Cre* pool, we also initiated tumours in a small cohort of *KT;H11<sup>LSL-Cas9/LSL-Cas9</sup>* mice. Reductions in the magnitude of the effects of various sgRNAs were observed in the *KT;H11<sup>LSL-Cas9/+</sup>* cohort relative to the *KT;H11<sup>LSL-Cas9/LSL-Cas9</sup>* cohort, underscoring the importance of matching Cas9 dosage and suggesting that Cas9 can be limiting in *H11<sup>LSL-Cas9/+</sup>* mice.

### Tuba-seq library generation

Genomic DNA was isolated from bulk tumour-bearing lung tissue from each mouse as previously described. Briefly, benchmark control cell lines were generated from LSL-YFP mouse embryonic fibroblasts transduced with a barcoded Lenti-sgNT3/Cre vector (NT3: an inert sgRNA with a distinct sgID) and purified by sorting YFP<sup>POS</sup> cells. Three benchmark control 'spike-in' cell lines (500,000 cells each) were added to each mouse lung sample before lysis to enable the calculation of the absolute number of neoplastic cells in each tumour from the number of sgID-BC reads. Following homogenization and overnight protease K digestion, genomic DNA was extracted from the lung lysates using standard phenol–chloroform and ethanol precipitation methods. Subsequently, Q5 High-Fidelity 2x Master Mix (New England Biolabs, M0494X) was used to amplify the sgID-BC region from 32 µg of genomic DNA in a total reaction volume of 800 µl per sample. The unique dual-indexed primers used were Forward: AAT GAT ACG GCG ACC ACC GAG ATC TAC AC-8 nucleotides for i5 index-ACA CTC TTT CCC TAC ACG ACG CTC TTC CGA TCT-6 to 9 random nucleotides for increased diversity-GCG CAC GTC TGC CGC GCT G and Reverse: CAA GCA GAA GAC GGC ATA CGA GAT-6 nucleotides for i7 index- GTG ACT GGA GTT CAG ACG TGT GCT CTT CCG ATC T-9 to 6 random nucleotides for increased diversity-CAG GTT CTT GCG AAC CTC AT. The PCR products were purified with Agencourt AMPure XP beads (Beckman Coulter, A63881) using a double size selection protocol. The concentration and quality of the purified libraries were determined using the Agilent High Sensitivity DNA kit (Agilent Technologies, 5067-4626) on the Agilent 2100 Bioanalyzer (Agilent Technologies, G2939BA). The libraries were pooled on the basis of lung weight to ensure even sequencing depth, cleaned up again using AMPure XP beads, and sequenced (read length 2 × 150 bp) on the Illumina HiSeq 2500 or NextSeq 500 platform (Admera Health Biopharma Services).

### Generation of stable cell lines

Parental cells were seeded at 50% confluency in a six-well plate the day before transduction (day 0). The cell culture medium was replaced with 2 ml fresh medium containing 8 µg ml<sup>-1</sup> hexadimethrine bromide (Sigma-Aldrich, H9268-5G), 20 µl ViralPlus Transduction Enhancer

(Applied Biological Materials, G698) and 40  $\mu$ l concentrated lentivirus, then cultured overnight (day 1). The medium was then replaced with complete medium and cultured for another 24 h (day 2). Cells were transferred into a 100 mm cell culture dish with appropriate amounts of antibiotic (blasticidin doses: U2OS: 10  $\mu$ g ml<sup>-1</sup>; HOP62: 50  $\mu$ g ml<sup>-1</sup>; H727: 10  $\mu$ g ml<sup>-1</sup>; H23: 15  $\mu$ g ml<sup>-1</sup>; puromycin doses: HC494: 5  $\mu$ g ml<sup>-1</sup>; U2OS: 1  $\mu$ g ml<sup>-1</sup>; HOP62: 5  $\mu$ g ml<sup>-1</sup>; H727: 5  $\mu$ g ml<sup>-1</sup>; H23: 5  $\mu$ g ml<sup>-1</sup>; 293T: 3  $\mu$ g ml<sup>-1</sup>) and selected for 48 h (day 3).

### Western blot

Cells were lysed in RIPA buffer (50 mM Tris-HCl (pH 7.4), 150 mM NaCl, 1% Nonidet P-40 and 0.1% SDS) and incubated at 4 °C with continuous rotation for 30 min, followed by centrifugation at 12,000 rcf for 10 min. The supernatant was collected, and the protein concentration was determined by BCA assay (Thermo Fisher Scientific, 23250). Protein extracts (10–50  $\mu$ g) were separated on 4–12% SDS-PAGE and transferred onto polyvinylidene fluoride membranes. The membranes were blocked with 5% non-fat milk in TBS with 0.1% Tween 20 (TBST) at room temperature for 1 h, cut according to the molecular weight of the target protein (with at least two flanking protein markers), followed by incubation with primary antibodies diluted in TBST (1:1,000) at 4 °C overnight. After three 10 min washes with TBST, the membranes were incubated with the appropriate secondary antibody conjugated to HRP diluted in TBST (1:10,000) at room temperature for 1 h. After three 10 min washes with TBST, protein expression was quantified with enhanced chemiluminescence reagents (Fisher Scientific, PI80196).

Antibodies used in this study: HSP90 (BD Biosciences, 610418), pAKT (Cell Signaling, 4060S), pERK (Cell Signaling, 4370L), ERK (Cell Signaling, 9102S), AKT (Cell Signaling, 4691S), HRAS (Thermo Fisher Scientific, 18295-1-AP), NRAS (Santa Cruz Biotechnology, sc-31), KRAS (EMD Millipore, OP-24), HA-tag (Cell Signaling, 2999S), Myc-tag (Cell Signaling, 2040S), Flag-tag (Cell Signaling, 86861S), BRAF (Cell Signaling, 14814S),  $\alpha$ -tubulin (Cell Signaling, 2144S), GAPDH (Cell Signaling, 5174S), goat-anti-rabbit IgG antibody, HRP-conjugate (Sigma-Aldrich, 12-348), and goat-anti-mouse IgG antibody, HRP-conjugate (Thermo Fisher Scientific, 62-6520). Recombinant RAS proteins used in this study: recombinant KRAS (Abcam, ab156968), recombinant HRAS (Abcam, ab93949) and recombinant NRAS (Abcam, ab268821).

### Co-immunoprecipitation assay

293T cells with stable expression of myc-KRAS<sup>G12D</sup> were transfected with plasmids expressing HA-tagged HRAS and Flag-tagged NRAS for 24 h before lysed with ice-cold immunoprecipitation lysis buffer (Thermo Fisher Scientific, 87788) containing protease inhibitor cocktail (Thermo Fisher Scientific 78442). The lysates were pre-cleared with magnetic beads (Thermo Fisher Scientific, 88802) at 4 °C for 2 h. Then protein concentration was determined by BCA assay (Thermo Fisher Scientific, 23250) and equal amount of protein lysis were incubated with anti-Myc- (Thermo Fisher Scientific, 88842) or IgG- (Cell Signaling, 5873S) magnetic beads at 4 °C for 12 h. The immunoprecipitates were collected using a MACSiMAG Separator (Miltenyi Biotec, 130-092-168), washed for three times with immunoprecipitation lysis buffer and three times with TBST. The immunoprecipitates were eluted via incubating in 1 $\times$  Non-Reducing Sample Buffer (Thermo Fisher Scientific, 39001) at 95 °C for 10 min before subjected to immunoblotting.

### Histology and immunohistochemistry

Lung lobes were fixed in 4% formalin and paraffin embedded. Haematoxylin and eosin (H&E) staining was performed using standard methods. Immunohistochemistry was performed on 4  $\mu$ m sections using the Avidin/Biotin Blocking Kit (Vector Laboratories, SP-2001), Avidin-Biotin Complex kit (Vector Laboratories, PK-4001) and DAB Peroxidase Substrate Kit (Vector Laboratories, SK-4100) following standard protocols.

The following primary antibodies were used: Ki-67 (BD Pharmingen, 550609, 1:100), bromodeoxyuridine (BrdU; BD Pharmingen, 555627, 1:100), human mitochondria (Abcam, ab92824, 1:100) and pERK (Cell Signaling, 4370 L, 1:50).

Total tumour burden (tumour area/total area  $\times$  100%), mitochondria<sup>pos</sup> tumour burden (mitochondria<sup>pos</sup> area/total area  $\times$  100%), BrdU<sup>pos</sup> cell number, Ki67<sup>pos</sup> cell number and pERK<sup>pos</sup> cell number were calculated using ImageJ 1.52p.

### Cell proliferation assay (CCK8)

For cell proliferation assays, cells were seeded in 96-well plates at a density of 5,000 cells per well and allowed to adhere overnight in regular growth medium (day 0). Cells were then cultured in medium as indicated on each figure panel for 7 days. Relative cell number were measured every other day using Cell Counting Kit-8 (Bimake, B34304) according to the manufacturer's instructions.

### Colony formation assay

For clonogenic assays, cells were seeded in six-well plates at a density of 500 cells per well and allowed to adhere overnight in regular growth medium. Cells were then cultured in medium as indicated on each figure panel for 14 days. Growth medium with or without drugs was replaced every 2 days. At the end point, cells were stained with 0.5% crystal violet in 20% methanol. Colony numbers were calculated using ImageJ.

### Xenograft studies in immunocompromised mice

For intravenous transplants into immunocompromised NSG mice, 5  $\times$  10<sup>5</sup> H23 cells were injected into one of the lateral tail veins. Mice were killed 28 days post-injection and lung lobes were fixed in 4% formalin and paraffin embedded. For subcutaneous transplants into immunocompromised NSG mice, 2  $\times$  10<sup>6</sup> each of H23 cells (sgSAFE, sgHRAS and sgNRAS) were resuspended in 200  $\mu$ l Matrigel<sup>®</sup> Basement Membrane Matrix (Corning, 354234) and injected into three parallel sites per mouse. Mice were killed 28 days post-injection. Tumours were dissected, and the weight, height, width and length of each tumour was measured. Tumour volume was roughly calculated via the following formula: Tumor volume = (4/3)  $\times$   $\pi$   $\times$  (Tumor length/2)  $\times$  (Tumor depth/2)  $\times$  (Tumor depth/2).

Maximal tumour size/burden permitted by Institute of Medicine Animal Care and Use Committee is 1.75 cm<sup>3</sup>, the maximal tumour size/burden was not exceeded in our study. Institute of Medicine Animal Care and Use Committee approved all animal studies and procedures.

### ReBiL2.0 assay

The ReBiL2.0 assay was performed as previously described<sup>16</sup>. 293T cells were co-transfected with plasmids expressing (1) nLuc- tethering with KRAS<sup>G12D</sup> or C20 (last 20 amino acids of KRAS); (2) cLuc tethering with KRAS<sup>G12D</sup> or C20 or wild-type H-/N-RAS; (3) myc-tagged RAS-GTPase; and (4) Renilla luciferase for 24 h. Transfected cells were seeded in (1) 96-well plates at a density of 2  $\times$  10<sup>4</sup> cells per well and (2) 6-well plates at a density of 1  $\times$  10<sup>6</sup> cells per well, and allowed to adhere overnight in regular growth medium (DMEM, 10% FBS). The next day, cells were cultured in serum limited medium (DMEM, 1% FBS) for 24 h. For experiment in Fig. 5e, stable ReBiL cells (U2OS-134-764np) were seeded in (1) 96-well plates at a density of 2  $\times$  10<sup>4</sup> cells per well, and (2) 6-well plates at a density of 1  $\times$  10<sup>6</sup> cells per well and allowed to adhere overnight in regular growth medium (DMEM/F12, 10% FBS and 10  $\mu$ g ml<sup>-1</sup> ciprofloxacin). The next day, cells were cultured in serum limited medium (DMEM/F12, 1% FBS and 10  $\mu$ g ml<sup>-1</sup> ciprofloxacin) containing 100 ng ml<sup>-1</sup> doxycycline for 24 h.

Upon termination of the ReBiL assay, (1) to measure raw luciferase activity, 300  $\mu$ M D-luciferin was added to 96-well plate cultures and incubated at 37 °C for 30 min, and raw luminescent data for both Renilla and firefly luciferase were collected by a Tecan microplate reader; (2)

to quantify the expression of 1/2luc fusion proteins, ReBiL cells from 6-well plate cultures were collected with RIPA lysis buffer for protein extraction, and western blots were performed for HA-tag, Myc-tag and HSP90 expression. Then the ReBiL2.0 score was calculated via the following formula:

$$\text{ReBiL2.0 score} = \left( \frac{[\text{Firefly}]}{[\text{Renilla}]} \right) / \left( \frac{[\text{Min}(\text{cLuc} - \text{HA}, \text{nLuc} - \text{HA})]}{[\text{HSP90}]} \right)$$

The strength of different RAS-GTPase in disrupting KRAS<sup>G12D</sup>-KRAS<sup>G12D</sup> interactions was calculated via the following formula:

$$\text{Strength} = \frac{[\text{ReBiL2.0}/(\text{Myc} - \text{tag}/\text{HSP90})]_{\text{RAS-GTPase}}}{[\text{ReBiL2.0}/(\text{Myc} - \text{tag}/\text{HSP90})]_{\text{KRASG12D}}}$$

### Analysis of human lung adenocarcinoma cancer genome sequencing data (for rare HRAS and NRAS mutations)

To assess evidence that *HRAS* and *NRAS* function as KRAS-specific tumour suppressors in human cancer, we queried publicly available cancer genomic datasets. GENIE Release 9.1-public was accessed through the Synapse platform and data on somatic mutations (data\_mutations\_extended.txt), sample- and patient-level clinical data (data\_clinical\_sample.txt and data\_clinical\_patient.txt), and genotyping panel information (genomic\_information.txt) were downloaded. While it is unclear how our findings may extrapolate to cancer types beyond lung adenocarcinoma, *HRAS* and *NRAS* mutations are rare (occurring at frequencies of just 0.83% and 2.87% in GENIE samples, respectively), so we performed a pan-cancer analysis. Each sample was assigned to its patient of origin and annotated for the presence of oncogenic *KRAS* mutations (defined as missense mutations in *KRAS* exons 12, 13 or 61) and for the presence of potentially functional *HRAS* or *NRAS* mutations (variants that were silent, intergenic or intronic, or fell in the 3' or 5' untranslated regions were excluded from this analysis). When multiple samples were derived from the same patient, the patient in question was annotated as having a mutation if it occurred in at least one of their associated samples. From this information we produced a list of the frequency of all *HRAS* and *NRAS* variants in patients with and without oncogenic *KRAS* in both datasets. The genotyping panel information was used to identify GENIE patients who were not genotyped at *HRAS* and/or *NRAS* and exclude these from the frequency calculation.

### Analysis of DepMap data

Cancer cell line dependency data (DepMap Public 19Q4) and mutation data (Cancer Cell Line Encyclopedia) were acquired from the Broad Institute DepMap Portal (<https://depmap.org/portal/>). Lung adenocarcinoma cell lines were identified by their Project Achilles identification code and partitioned into *KRAS* mutant, if they contained a hotspot mutation, or wild-type groups. Subsequently, dependency scores for *NRAS* or *KRAS* were calculated for each cell line within the two groups. Finally, the distributions of dependency scores were plotted using GraphPad Prism 9.

### Processing of paired-end reads to identify the sgID and BC

Sequencing of Tuba-seq libraries produces reads that are expected to contain an 8-nucleotide sgID followed by a 30-nucleotide BC of the form GCNNNNNTANNNNNGCNNNNNTANNNNNGC, where each of the 20 Ns represents a random nucleotide. Each sgID has a one-to-one correspondence with an sgRNA in the viral pool; thus, the sgID sequence identifies the gene targeted in a given tumour. Note that all sgID sequences in the viral pool differ from each other by at least three nucleotides such that incorrect sgID assignment (and thus, inference of tumour genotype) due to PCR or sequencing error is extremely

unlikely. The random 20-nucleotide portion of the BC is expected to be unique to each lentiviral integration event and, thus, tags all cells in a single clonal expansion. Note that the length of the BC ensures a high theoretical potential diversity ( $\sim 4^{20} > 10^{12}$  BCs per vector), so while the actual diversity of each Lenti-sgRNA/Cre vector is dictated by the number of colonies generated during the plasmid barcoding step, it is very unlikely that we will observe the same BC in multiple clonal expansions.

FASTQ files were parsed using regular expressions to identify the sgID and BC for each read. To minimize the effects of sequencing error on BC identification, we required the forward and reverse reads to agree completely within the 30-nucleotide sequence to be further processed. We also screened for BCs that were likely to have arisen due to errors in sequencing the BCs of genuine tumours. Given the low rate of sequencing error, we expect these spurious 'tumours' to have read counts that are far lower than the read counts of the genuine tumours from which they arise. While it is impossible to eliminate these spurious tumours, we sought to minimize their effect by identifying small 'tumours' with BCs that are highly similar to the BCs of larger tumours. Specifically, if a pair of 'tumours' had BCs that were within a Hamming distance of two, and if one of the tumours had fewer than 5% as many reads as the other, then the reads associated with the smaller tumour were attributed to the larger tumour. After these filtering steps, the read counts associated with each BC were converted to absolute neoplastic cell numbers by normalizing to the number of reads from the 'spike-in' cell lines added to each sample before lung lysis and DNA extraction. The median sequencing depth across experiments was  $\sim 1$  read per 6.4 cells.

For statistical comparisons of tumour genotypes, we applied a minimum tumour size cut-off of 100 cells. In selecting a cut-off, we sought to include tumours that are large enough to be consistently detected despite differences in sequencing depth among mice, while using as many tumours as possible to maximize the statistical power. Importantly, we analysed each Tuba-seq dataset with multiple minimum tumour size cut-offs (50, 100, 200 and 500 cells) and found that our findings were robust.

### Summary statistics for overall growth rate

To assess the extent to which a given gene (*X*) affects tumour growth, we compared the distribution of tumour sizes produced by vectors targeting that gene (sg*X* tumours) to the distribution produced by our negative control vectors (sgInert tumours). We relied on two statistics to characterize these distributions: the size of tumours at defined percentiles of the distribution (specifically the 50th, 60th, 70th, 80th, 90th and 95th percentile tumour sizes), and the log-normal mean size (LN mean). The percentile sizes are non-parametric summary statistics of the tumour size distribution. In considering percentiles corresponding to the right tail of the distribution, we focus on the growth of larger tumours, thereby avoiding issues stemming from potential variation in cutting efficiency among guides. The LN mean is the maximum-likelihood estimate of mean tumour size assuming a log-normal distribution. Previous work found that this statistic represents the best parametric summary of tumour growth based on the maximum likelihood quality of fit of various common parametric distributions.

To quantify the extent to which each gene suppressed or promoted tumour growth, we normalized statistics calculated on tumours of each genotype to the corresponding statistic. The resulting ratios reflect the growth advantage (or disadvantage) associated with each tumour genotype relative to the growth of sgInert tumours.

For example, the relative *i*th percentile size for tumours of genotype *X* was calculated as:

$$\text{Relative size at } i^{\text{th}} \text{ percentile}_{\text{sgX}} = \frac{i^{\text{th}} \text{ percentile of sgX distribution}}{i^{\text{th}} \text{ percentile of sgInert distribution}}$$

Likewise, the relative LN mean size for tumours of genotype  $X$  was calculated as:

$$\text{Relative LNmean}_{\text{sg}X} = \frac{\text{LNmean of sg}X \text{ distribution}}{\text{LNmean of sgInert distribution}}$$

### Summary statistics for relative tumour number and relative tumour burden

In addition to the tumour size metrics described above, we characterized the effects of gene inactivation on tumorigenesis in terms of the number of tumours and total neoplastic cell number ('tumour burden') associated with each genotype. Unlike the aforementioned metrics of tumour size, tumour number and burden are linearly affected by lentiviral titre and are thus sensitive to underlying differences in the representation of each Lenti-sgRNA/Cre vector in the viral pool. Critically, each Tuba-seq experiment included a cohort of  $KT$  control mice. As  $KT$  mice lack expression of Cas9, all Lenti-sgRNA/Cre vectors are functionally equivalent in these mice, and the observed tumour number and burden associated with each sgRNA reflects the make-up of the viral pool.

To assess the extent to which a given gene ( $X$ ) affects tumour number, we first normalized the number of sg $X$  tumours in  $KT;H11^{LSL-Cas9}$  mice (also  $KT;p53^{\text{lox/lox}};H11^{LSL-Cas9}$  and  $Braf^{LSL-V600E/+};H11^{LSL-Cas9}$  mice in the initial Kras-interacting protein screen and the paired screen, respectively) to the number of sg $X$  tumours in the  $KT$  mice:

$$\text{Tumour number}_{\text{sg}X} = \frac{\text{Number of sg}X \text{ tumours in } KT; H11^{LSL-Cas9} \text{ mice}}{\text{Number of sg}X \text{ tumours in } KT \text{ mice}}$$

As with the tumour size metrics, we then calculated a relative tumour number by normalizing this statistic to the corresponding statistic calculated using sgInert tumours:

$$\text{Relative tumour number}_{\text{sg}X} = \frac{\text{Tumour number}_{\text{sg}X}}{\text{Tumour number}_{\text{sgInert}}}$$

Genes that influence relative tumour number modify the probability of tumour initiation and/or the very early stages of oncogene-driven epithelial expansion, which prior work suggests are imperfectly correlated with tumour growth at later stages. Relative tumour number thus captures an additional and potentially important aspect of tumour suppressor gene function.

Analogous to the calculation of relative tumour number, we characterized the effect of each gene on tumour burden by first normalizing the sg $X$  tumour burden in Cas9-expressing mice to the burden in  $KT$  mice:

$$\text{Tumour burden}_{\text{sg}X} = \frac{\text{Total neoplastic cell number for sg}X \text{ in } KT;H11^{LSL-Cas9} \text{ mice}}{\text{Total neoplastic cell number for sg}X \text{ in } KT \text{ mice}}$$

We then calculated relative tumour burden by normalizing this number to the corresponding statistic calculated using sgInert tumours:

$$\text{Relative tumour burden}_{\text{sg}X} = \frac{\text{Tumour burden}_{\text{sg}X}}{\text{Tumour burden}_{\text{sgInert}}}$$

Tumour burden is an integration of tumour size and number, and thus reflects the total neoplastic load in each mouse. Tumour burden is thus more strongly related to morbidity than are our metrics of tumour size and is closely related to traditional measurements of tumour progression such as duration of survival and tumour area. While intuitively appealing, tumour burden is notably noisier than our

metrics of tumour size as it is strongly determined by the size of the largest tumours.

### Calculation of confidence intervals and $P$ values for tumour growth and number metrics

Confidence intervals and  $P$  values were calculated using bootstrap resampling to estimate the sampling distribution of each statistic. To account for both mouse-to-mouse variability and variability in tumour size and number within mice, we adopted a two-step, nested bootstrap approach where we first resampled mice, and then resampled tumours within each mouse in the pseudo-dataset. A total of 10,000 bootstrap samples were drawn for all reported  $P$  values. The 95% confidence intervals were calculated using the 2.5th and 97.5th percentile of the bootstrapped statistics. As we calculate metrics of tumour growth that are normalized to the same metrics in sgInert tumours, under the null model where genotype does not affect tumour growth, the test statistic is equal to 1. Two-sided  $P$  values were thus calculated as follows:

$$P = 2 \times \min\{\text{Pr}(T > 1), \text{Pr}(T < 1)\}$$

where  $T$  is the test statistic and  $\text{Pr}(T > 1)$  and  $\text{Pr}(T < 1)$  were calculated empirically as the proportion of bootstrapped statistics that were more extreme than the baseline of 1. To account for multiple hypothesis testing,  $P$  values were false discovery rate (FDR)-adjusted using the Benjamini–Hochberg procedure as implemented in the Python package stats models. Summarized statistics of all Tuba-seq experiments in this study can be found in Supplementary Tables 3–6.

### AP/MS data visualization

AP/MS data were analysed as described<sup>57</sup>. Briefly, protein spectral matches<sup>10</sup> were normalized by protein length and total spectral matches per experiment. These normalized spectral abundance factors (NSAFs) were then normalized to NSAFs of matched prey proteins from a large cohort of unrelated AP/MS experiments to produce a  $Z$ -score.  $Z$ -scores are proportional to the areas of circles in bubble plots. In cluster diagrams, NSAFs are binarized by statistical significance (FDR > 0.5), similarities between interactome profiles were determined by cosine distance, and dendrogram topology was determined by unweighted pair group method with arithmetic mean.

### Modelling RAS–RAS dimers

Potential templates for modelling RAS heterodimers were obtained from the ProtCID database. ProtCID is built from clustering interfaces of homologous proteins obtained from domain–domain contacts within protein crystals in the Protein Data Bank. Hierarchical clustering of interfaces is performed with a Jaccard-index similarity metric based on the contacts shared between different interfaces. Models for the structure of the HRAS/KRAS heterodimer were built by superimposing a structure of KRAS<sup>G12D</sup> (PDB: 5USJ) onto a monomer of the HRAS homodimer in PDB entry 3K8Y. All structural data files generated in this study can be accessed via Zenodo (<https://zenodo.org/record/7104280>).

### Statistical analysis for non-Tuba-seq experiments

Sample or experiment sizes were estimated on the basis of similar experiments previously performed in our laboratory, as well as in the literature. Biological replications (more than five mice for each cohort, more than ten wells per culture condition) of the experiments were as detailed in the figures. All values are presented as mean  $\pm$  standard deviation (s.d.), with individual data points shown in the figure when possible. Comparisons of parameters between two groups were made by two-tailed Student's  $t$ -tests. The differences among several groups were evaluated by one-way analysis of variance (ANOVA) with Tukey–Kramer post hoc evaluation.  $P$  values less than 0.05 and 0.01 were considered significant (\*) or very significant (\*\*), respectively.

## Statistics and reproducibility

The statistical tests used for each analysis are described in detail in the sections above. All analyses of BC sequencing data were performed in Python (3.4), and visualizations of data were performed in R (3.6.0). Sample sizes were determined on the basis of our previous experience conducting similar experiments and, in the case of Tuba-seq experiments, on the basis of previously published power analyses<sup>18</sup>. For experiments using western blot as a readout, at least three independent experiments were repeated with similar results. In all the experiments reported in this study, no data points were excluded. No randomization was used in this study. Data collection and analysis were not performed blind to the conditions of the experiments. Analyses of BC sequencing data used non-parametric statistics; therefore, no assumptions about the distribution of data were made. For all other analyses, data distributions were assumed to be normal, but this was not formally tested, and individual data points are plotted to show distribution.

## Reporting summary

Further information on research design is available in the Nature Portfolio Reporting Summary linked to this article.

## Data availability

The human cancer genomic data analysed for the presence of rare HRAS and NRAS variants in this manuscript were derived from the AACR's Project GENIE (<https://www.aacr.org/professionals/research/aacr-project-genie/>) Release 9.1-public dataset. All data files that support the findings of this study are available through the Synapse platform (<https://www.synapse.org/#!Synapse:syn24179657>). Human cancer genomic data analysed for alterations in KRAS-interacting proteins were derived from the TCGA PanCancer Atlas dataset, which is publicly available through cBioPortal at [https://www.cbioportal.org/study/summary?id=luad\\_tcga\\_pan\\_can\\_atlas\\_2018](https://www.cbioportal.org/study/summary?id=luad_tcga_pan_can_atlas_2018). The protein templates used to model RAS heterodimers in this study are available through the ProtCID database (KRAS<sup>G12D</sup>: PDB entry 5USJ, HRAS homodimer: PDB entry 3K8Y), and resulting structural data files can be accessed through Zenodo (<https://zenodo.org/record/7104280>). AP/MS data were derived from ref. 10 (PMID: 32727735) and ref. 11 (PMID: 32929263). Gene expression data were derived from ref. 21 (PMID: 28191885). Pre-existing CRISPR/Cas9 screen data were derived from ref. 15 (PMID: 32238925). All BC sequencing datasets are available through the NCBI's Sequence Read Archive database under the BioProject accession number PRJNA763983 (<https://www.ncbi.nlm.nih.gov/sra/PRJNA763983>). Processed data plotted in figures are available in the Extended Data Information. All other data supporting the findings of this study are available from the corresponding author on reasonable request. Source data are provided with this paper.

## Code availability

The code used for data analysis in this study is available on GitHub (<https://github.com/eshuldiner/KrasIP>).

## References

- Ding, S. et al. Comparative proteomics reveals strain-specific  $\beta$ -TrCP degradation via rotavirus NSP1 hijacking a host cullin-3-Rbx1 complex. *PLoS Pathog.* **12**, e1005929 (2016).
- Xu, Q. & Dunbrack, R. L. ProtCID: a data resource for structural information on protein interactions. *Nat. Commun.* **11**, 711 (2020).
- Alford, R. F. et al. The Rosetta all-atom energy function for macromolecular modeling and design. *J. Chem. Theory Comput.* **13**, 3031–3048 (2017).
- Shapovalov, M. V. & Dunbrack, R. L. Jr A smoothed backbone-dependent rotamer library for proteins derived from adaptive kernel density estimates and regressions. *Structure* **19**, 844–858 (2011).

## Acknowledgements

We thank the Stanford Veterinary Animal Care Staff for expert animal care; Human Pathology/Histology Service Center, Stanford Protein and Nucleic Acid Facility for experimental support; and A. Orantes for administrative support; Members of the Winslow laboratory and I. Prior for helpful comments. R.T. was supported by a Tobacco-Related Disease Research Program (TRDRP) postdoctoral fellowship (27FT-0044), a Stanford Cancer Institute fellowship, a Stanford-Rambam Health Care collaboration grant (259348) and an NCI K99/R00 pathway to independence grant (K99CA256039). C.W.M. was supported by the NSF Graduate Research Fellowship Program and an Anne T. and Robert M. Bass Stanford Graduate Fellowship. J.D.H. was supported by a Stanford University School of Medicine Dean's Postdoctoral Fellowship and a TRDRP Postdoctoral fellowship (T31FT1619). H.C. was supported by a TRDRP Postdoctoral Fellowship (28FT-0019). N.W.H. was supported by the NSF Graduate Research Fellowship Program. M.I.P. was supported by an NIH F30 fellowship (GM142263). Work in the laboratory of R.L.D. was supported by the Fox Chase Cancer Center Support Grant (NIH P30 CA006927). Work in the laboratory of G.M.W. was supported, in part, by Cancer Center Core Grant CA014195, the Breast Cancer Research Foundation, the Freeberg Foundation and the NIH/National Cancer Institute (Grant R35 CA197687). This work was supported by NIH R01-CA230025 (to M.M.W.), NIH R01-CA231253 (to M.M.W. and D.A.P.), NIH R01-CA234349 (to M.M.W. and D.A.P.), TRDRP 27IP-0052 (to M.M.W.), R01-CA250534 (to P.K.J.), R35-GM122517 (to R.L.D.) and in part by the Stanford Cancer institute support grant (NIH P30-CA124435). The funders had no role in study design, data collection and analysis, decision to publish or preparation of the manuscript.

## Author contributions

R.T., E.G.S. and M.M.W. conceived the project and designed the experiments. R.T. led experimental data production with contributions from E.G.S., M.K., C.W.M., J.D.H., L.A., M.K.T., N.W.H., M.I.P., H.C., Y.-C.L. and G.M.W. R.T. and E.G.S. led the data analysis. E.G.S. performed the Tuba-seq analysis. M.K. and P.K.J. performed AP/MS data analysis. M.I.P. and R.L.D. performed RAS–RAS dimer modelling. D.A.P. and M.M.W. oversaw the project. R.T., E.G.S. and M.M.W. wrote the manuscript with input from all authors.

## Competing interests

M.M.W. and D.A.P. are co-founders of, and hold equity in, D2G Oncology, Inc. The other authors declare no competing interests.

## Additional information

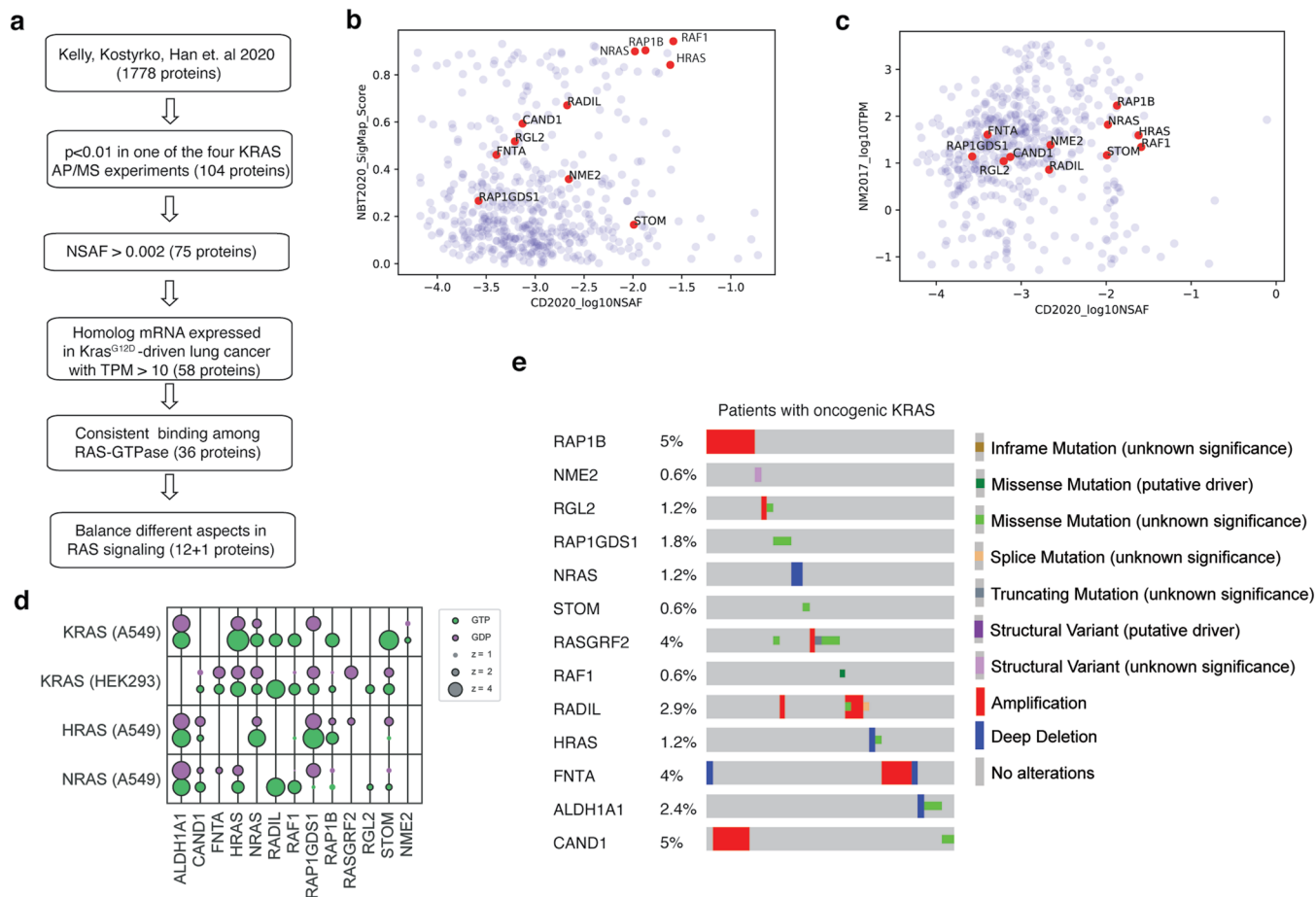
**Extended data** is available for this paper at <https://doi.org/10.1038/s41556-022-01049-w>.

**Supplementary information** The online version contains supplementary material available at <https://doi.org/10.1038/s41556-022-01049-w>.

**Correspondence and requests for materials** should be addressed to Monte M. Winslow.

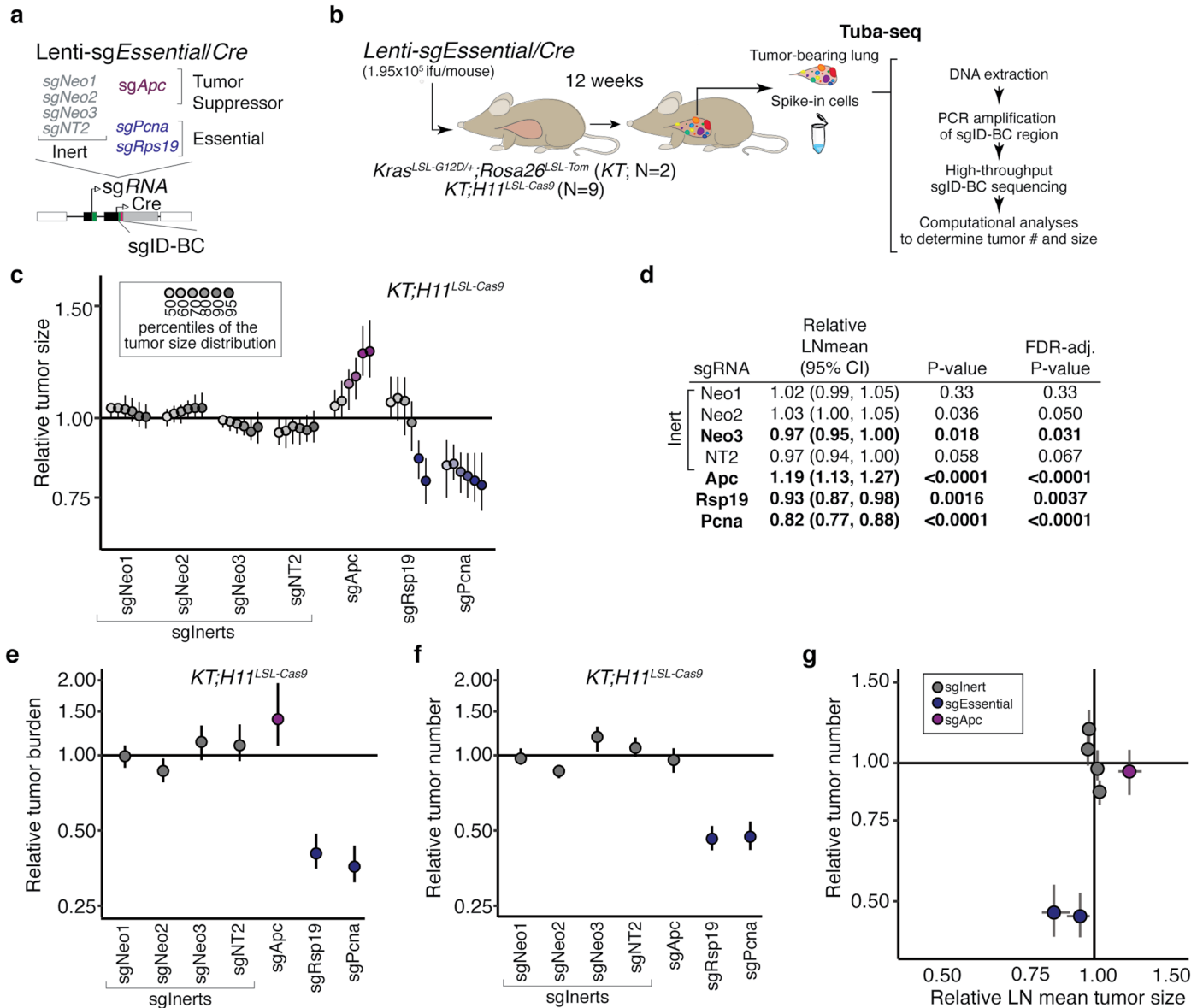
**Peer review information** *Nature Cell Biology* thanks Mark Philips, Hongbin Ji and the other, anonymous, reviewer(s) for their contribution to the peer review of this work.

**Reprints and permissions information** is available at [www.nature.com/reprints](http://www.nature.com/reprints).



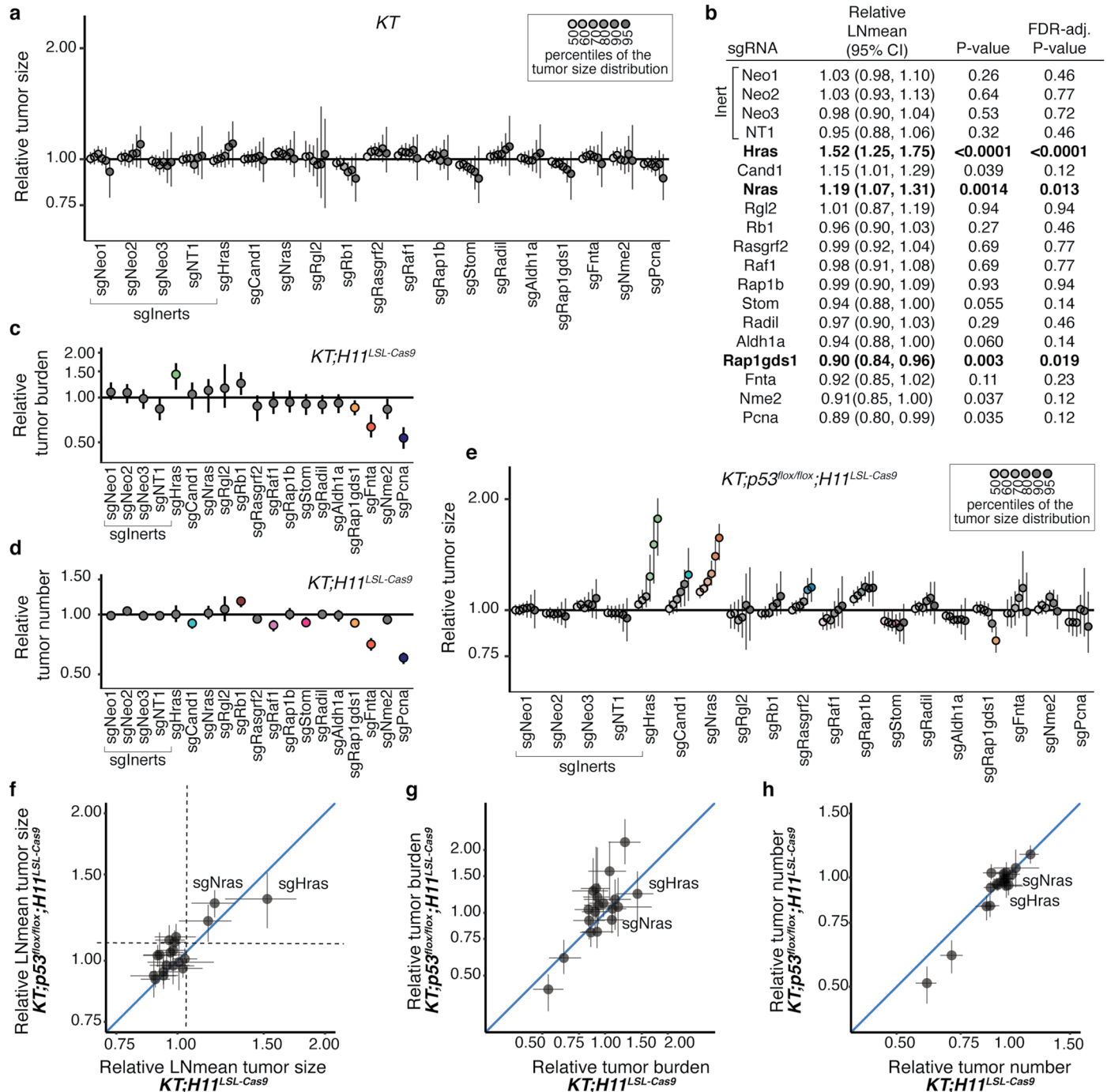
**Extended Data Fig. 1 | Prioritization of candidate KRAS-interacting proteins for this study.** **a.** Flow chart for prioritization of candidate KRAS-interacting proteins for this study. Candidate KRAS-interacting proteins were chosen based on multiple criteria including their interaction with KRAS, their homolog mRNA expression in a mouse model of *Kras*<sup>G12D</sup>-driven lung cancer, and the consistency with which they bind different RAS-GTPases. RADIL was added at the last step due to its validated importance in KRAS-mutant human cell lines. **b.** Candidate proteins interact with KRAS in two protein-protein interaction analyses (Kelly, Kostyrko, Han et al. 2020; Broyde, Simpson, Murray et al. 2020).

KRAS-interacting proteins are shown as their log10NSAF and SigMap Scores. **c.** Homolog mRNA expression (TPM) of candidate KRAS-interacting proteins in a mouse model of *Kras*<sup>G12D</sup>-driven lung cancer (Chuang et al. 2017). **d.** Bubble plot of eight AP/MS experiments with GTP- and GDP-locked mutant GTPases as baits (rows), showing the enrichment of selected candidate KRAS-interacting proteins (columns). Dark borders indicate FDR < 0.05. **e.** Mutation and copy number alteration frequencies of the 13 candidate genes in lung adenocarcinomas with oncogenic KRAS (N = 152; data from TCGA PanCancer Atlas, Cell 2018).



**Extended Data Fig. 2 | Tumor barcoding coupled with barcode sequencing (Tuba-seq) can uncover engineered alterations that reduce tumor number and growth. a-b.** Schematic of the Tuba-seq approach to measure the effects of essential gene inactivation on tumor growth. Tumors were initiated with pool of barcoded lentiviral-sgRNA/Cre vectors targeting known essential genes and tumor suppressor *Apc* (Lenti-sgEssential/Cre) in *KT* and *KT;H11<sup>LSL-Cas9</sup>* mice (a). Tuba-seq was performed on each tumor-bearing lung 12 weeks after initiation (b). **c.** Points denote tumor sizes at indicated percentiles for each sgRNA relative to the size of sgInert-containing tumors at the corresponding percentiles. Percentiles that are significantly different from sgInert (two-sided FDR-corrected  $p < 0.05$ ) are in color. **d.** The impact of each sgRNA on mean tumor size relative to sgInerts, assuming a log-normal distribution of tumor sizes (LNmean). sgRNAs with two-sided FDR-corrected  $P < 0.05$  are in bold. **e.** Points denote the impact

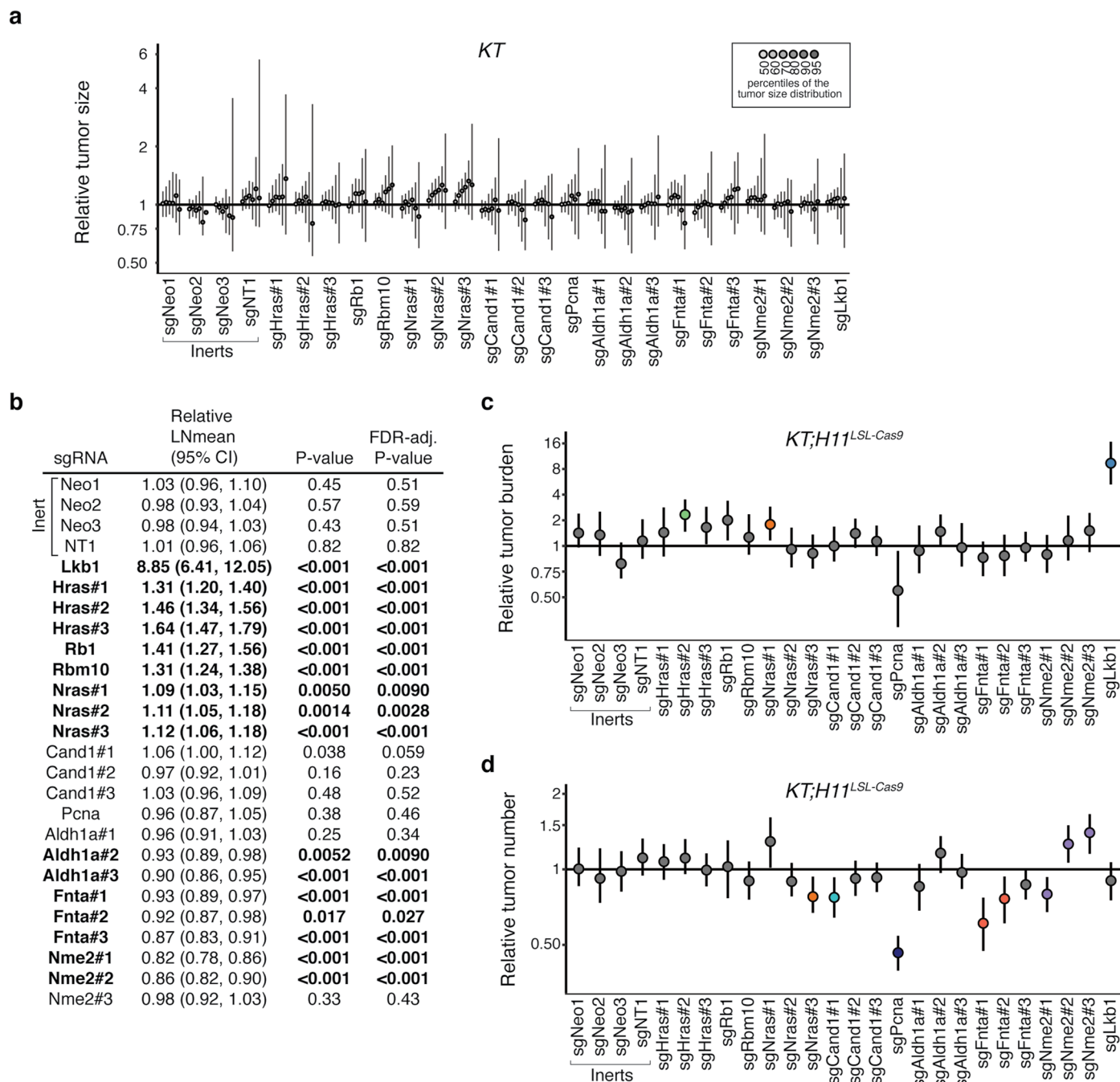
of each sgRNA on tumor burden relative to sgInerts and normalized to the same statistic in *KT* mice. Relative burdens significantly different from sgInert (two-sided FDR-corrected  $p < 0.05$ ) are in color. **f.** Points denote the impact of each sgRNA on tumor number relative to sgInerts and normalized to the same statistic in *KT* mice. Relative tumor numbers significantly different from sgInert (two-sided FDR-corrected  $p < 0.05$ ) are in color. **g.** Points denote the impact of each sgRNA on tumor number plotted against its impact on LNmean tumor size. The lines at  $y = 1$  and  $x = 1$  indicate no effect relative to sgInert on tumor number and size, respectively. For panels c and e-g: Error bars indicate 95% confidence intervals around point estimates of the test statistic. Confidence intervals and P-values were calculated using a nested bootstrap resampling approach across 9 *KT;H11<sup>LSL-Cas9</sup>* mice and 2 *KT* mice. sgInerts are in gray and the line at  $y = 1$  indicates no effect.



**Extended Data Fig. 3 | Inactivation of KRAS-interacting proteins has similar impacts on tumor growth in p53-proficient and p53-deficient contexts.**

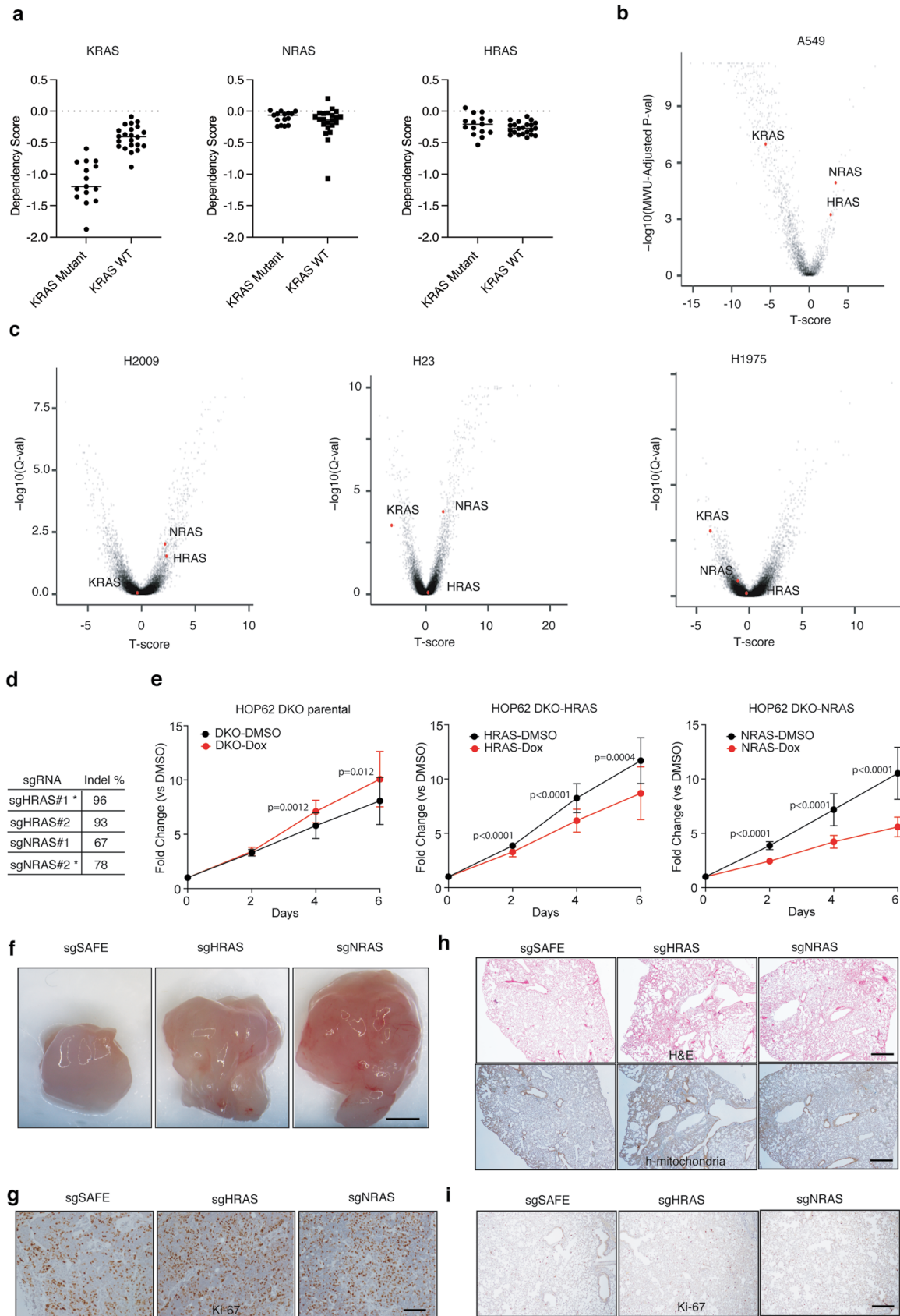
**a.** Points denote tumor sizes at indicated percentiles for each sgRNA relative to the size of sgInert-containing tumors at the corresponding percentiles in *KT* mice. Genes are ordered as in Fig. 1f. Line at  $y = 1$  indicates no effect relative to sgInert. As expected, no percentiles were significantly different from sgInert (two-sided FDR-adjusted  $p < 0.05$ ). **b.** The impact of each sgRNA on mean tumor size relative to sgInerts in *KT;H11<sup>LSL-Cas9</sup>* mice, assuming a log-normal distribution of tumor sizes (LNmean). sgRNAs with two-sided  $P < 0.05$  after FDR-adjustment are in bold. **c-d.** Points denote the impact of each sgRNA on tumor burden (c) and number (d) relative to sgInerts in *KT;H11<sup>LSL-Cas9</sup>* mice, normalized to the corresponding statistic in *KT* mice to account for representation of each sgRNA in the viral pool. sgInerts are in gray and the line at  $y = 1$  indicates no effect. Relative

tumor burdens and numbers significantly different from sgInert (two-sided FDR-adjusted  $p < 0.05$ ) are in color. **e.** Points denote tumor sizes at the indicated percentiles for each sgRNA relative to the size of sgInert-containing tumors in *KT;p53<sup>fllox/fllox</sup>;H11<sup>LSL-Cas9</sup>* mice. Genes are ordered as in Fig. 1f. The line at  $y = 1$  indicates no effect relative to sgInert. Percentiles that are significantly different from sgInert (two-sided FDR-adjusted  $p < 0.05$ ) are in color. **f-h.** Comparison of the impact of each sgRNA on relative LNmean tumor size (f), tumor burden (g) and tumor number (h) in *KT;H11<sup>LSL-Cas9</sup>* and *KT;p53<sup>fllox/fllox</sup>;H11<sup>LSL-Cas9</sup>* mice. For all panels: Error bars indicate 95% confidence intervals around point estimates of the test statistics. Confidence intervals and P-values were calculated using a nested bootstrap resampling approach described across 11 *KT;H11<sup>LSL-Cas9</sup>* mice, 6 *KT;p53<sup>fllox/fllox</sup>;H11<sup>LSL-Cas9</sup>* mice and 5 *KT* mice.



**Extended Data Fig. 4 | Top candidate KRAS-interacting proteins from initial Tuba-seq screen impact multiple metrics of tumor growth in validation cohort. a.** Points denote tumor sizes at indicated percentiles for each sgRNA relative to the size of sgInert-containing tumors at the corresponding percentiles in *KT* mice. *KT* genes lack Cas9, thus all sgRNAs are functionally equivalent to sgInerts. Genes are ordered as in Fig. 2d, but note the change in axis scaling. Line at  $y = 1$  indicates no effect relative to sgInerts. As expected, no percentiles were significantly different from sgInert (FDR-adjusted  $p < 0.05$ ). **b.** The impact of each sgRNA on mean tumor size relative to sgInerts, assuming a log-normal distribution of tumor sizes (LNmean). sgRNAs with two-sided  $P < 0.05$  after FDR-adjustment are in bold. Note that these data for the sgInerts, sgHras#1-3 and sgNras#1-3 are also plotted in Fig. 2e. **c.** Points denote the impact of each sgRNA on tumor burden relative to sgInerts in *KT;H11<sup>LSL-Cas9</sup>* mice, normalized

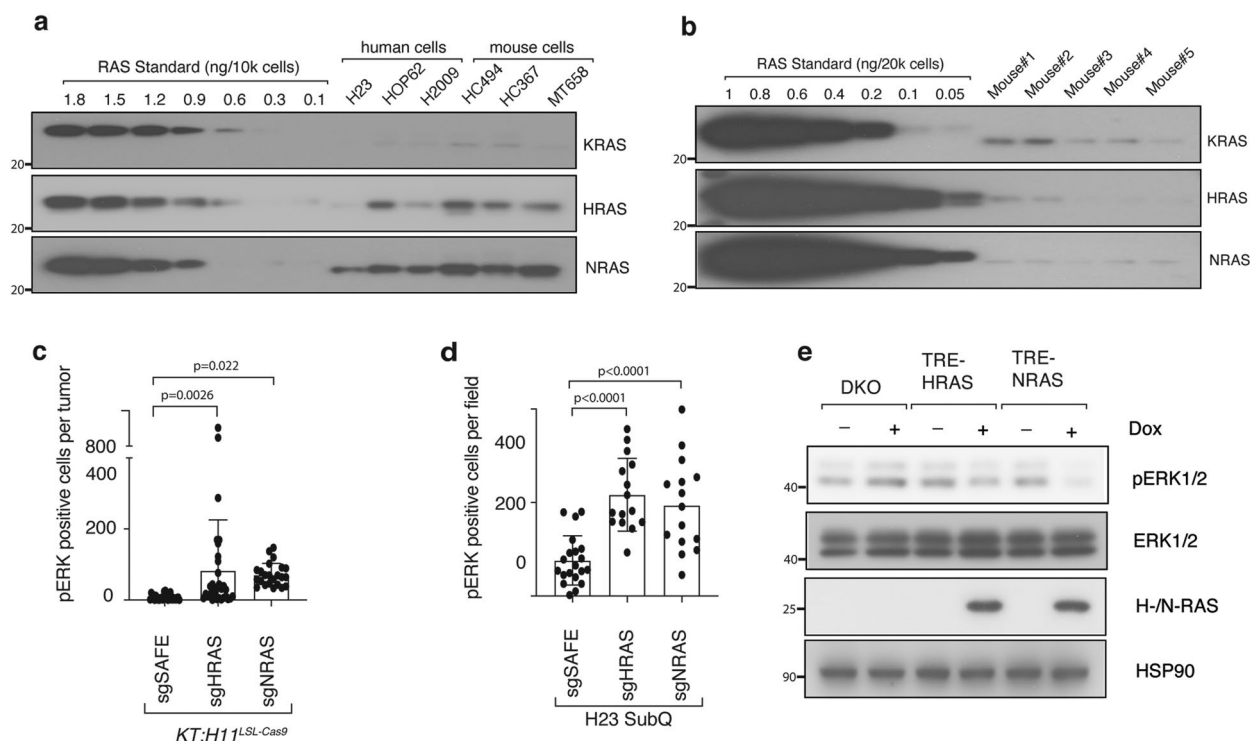
to the corresponding statistic in *KT* mice to account for the representation of each sgRNA in the viral pool. sgInerts are in gray and the line at  $y = 1$  indicates no effect. Relative tumor burdens significantly different from sgInert (two-sided FDR-adjusted  $p < 0.05$ ) are in color. **d.** Points denote the impact of each sgRNA on tumor number relative to sgInerts in *KT;H11<sup>LSL-Cas9</sup>* mice, normalized to the corresponding statistic in *KT* mice to account for representation of each sgRNA in the viral pool. sgInerts are in gray and the line at  $y = 1$  indicates no effect. Relative tumor numbers significantly different from sgInert (two-sided FDR-adjusted  $p < 0.05$ ) are in color. For all panels: Error bars indicate 95% confidence intervals around point estimates of the test statistic. Confidence intervals and P-values were calculated using a nested bootstrap resampling approach across 20 *KT;H11<sup>LSL-Cas9</sup>* mice and 4 *KT* mice.



Extended Data Fig. 5 | See next page for caption.

**Extended Data Fig. 5 | Wild type RAS paralogs constrain the growth of human KRAS-driven cancer cell lines.** **a.** RAS family member dependency scores in human lung adenocarcinoma (LUAD) cell lines. **b.** Effects of RAS gene knockouts in A549 cells. The T-score represents the normalized effect of multiple sgRNAs targeting a gene. A positive T-score indicates a tumor-suppressive effect. The effects of each gene relative to SAFE sgRNAs were tested via Mann–Whitney U test, corrected via Benjamini–Hochberg procedure. (Data source: Kelly, Kostyrko, Han *et al.* 2020). **c.** Effects of RAS gene knockouts in KRAS-mutant human LUAD cells in 3D culture. The effects of each gene relative to SAFE sgRNAs were tested via two-sided Benjamini–Hochberg-corrected t-test. (Data source: Han *et al.* 2020). **d.** Indel rates in cell lines with the indicated sgRNAs. \* denotes sgRNAs used for cell culture and transplantation experiments. **e.** Re-expression of wild-type HRAS or NRAS suppresses proliferation of HRAS and NRAS double

knockout (DKO) HOP62 cells. Cells were seeded in 96-well plates and cultured under limited serum (1%) with or without Doxycycline (Dox). Cell numbers were measured via CCK8 assay. Points are Mean±SD of 16 wells normalized to Day 0. (one-tailed t-test). **f.** Representative images of subcutaneous tumors 4 weeks after transplantation with H23 cells. Quantification is in Fig. 3h. Scale bar: 2 mm. **g.** Representative images of Ki67 staining from subcutaneous tumors four weeks after transplantation with H23 cells. Quantification is shown in Fig. 3i. Scale bar: 100 µm. **h.** Representative images of H&E and human mitochondria staining on lung tumors 4 weeks after intravenous transplantation with H23 cells. Quantification is in Fig. 3j. Scale bar: 500 µm. **i.** Representative images of Ki67 staining from lung tumors 4 weeks after intravenous transplantation with H23 cells. Quantification is in Fig. 3k. Scale bar: 200 µm.



**Extended Data Fig. 6 | Wild-type RAS paralogs finetune RAS signaling. a.** Western blot analysis of three RAS paralogs' expression per 10,000 human and mouse KRAS-driven lung cancer cell lines. Recombinant RAS proteins were used as a standard. **b.** Western blot analysis of three RAS paralogs' expression per 20,000 sorted *Braf*<sup>V600E</sup>-driven mouse lung cancer cells. Recombinant RAS proteins were used as a standard. **c.** Quantification of pERK<sup>pos</sup> cells in *KT;H1<sup>LSL-Cas9</sup>* mice with tumors initiated with Lenti-sgRNA/Cre vectors as indicated in Fig. 4a. Each dot represents a tumor. (one-way ANOVA). **d.** Quantification of pERK<sup>pos</sup> cells per field of indicated cells from Fig. 4b. Each dot represents a view field.

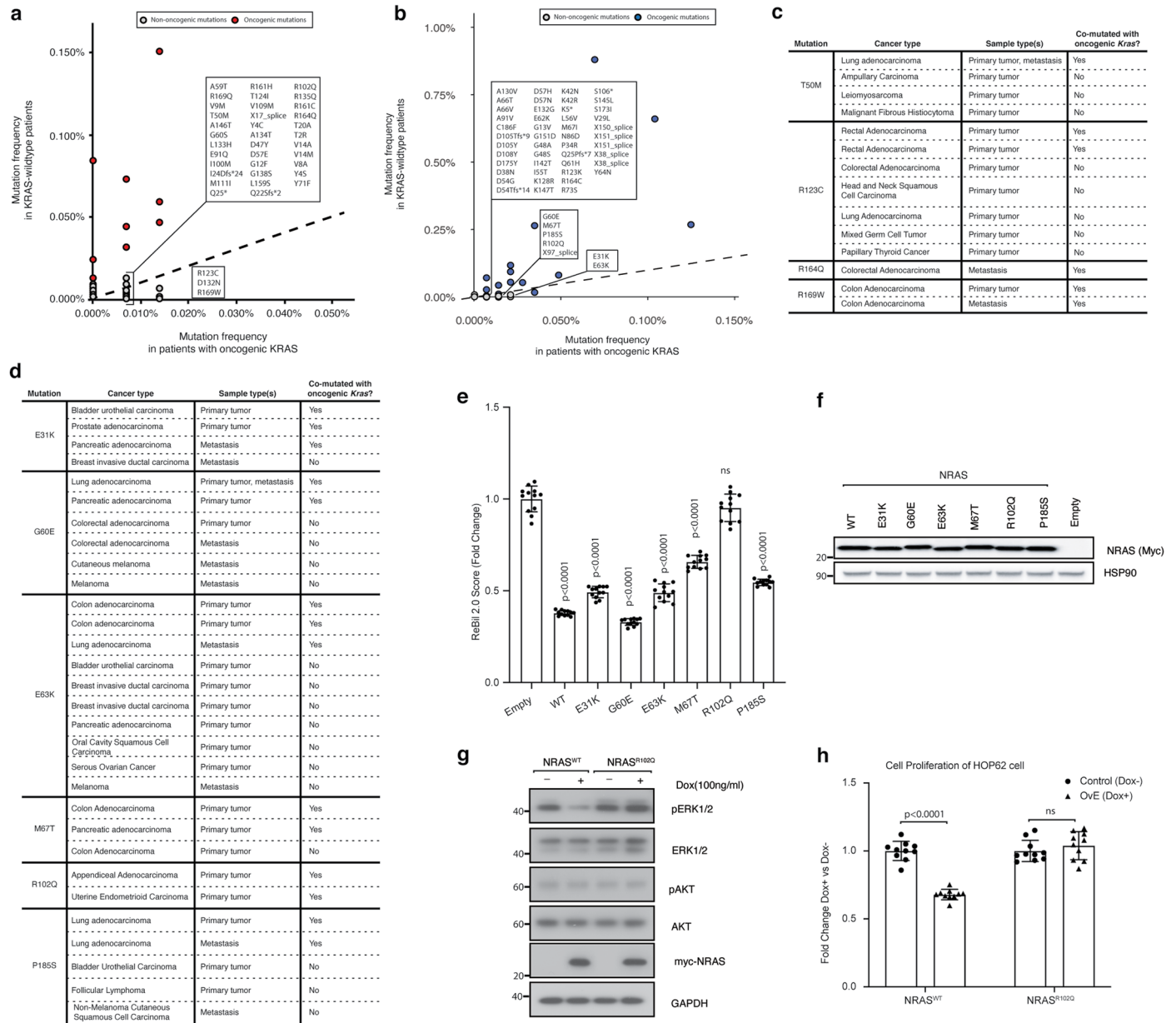
(one-way ANOVA). SubQ, subcutaneous. **e.** Western blot analysis of *HRAS* and *NRAS* double knockout (DKO) HOP62 cells re-expressing *HRAS* (TRE-*HRAS*) or *NRAS* (TRE-*NRAS*) under Doxycycline (Dox) treatment. DKO cells were generated as described in Fig. 3a. DKO cells were re-transduced with lentiviral vector expressing TRE-*HRAS* or TRE-*NRAS* at high MOI (> 5) to generate stable re-expressing cells. To re-express *HRAS*, cells were treated with 10 ng/ml Dox. To re-express *NRAS*, cells were treated with 50 ng/ml Dox. All cells were cultured under limited serum (1%) for 2 days before protein extraction. HSP90 is blotted as loading control.



**Extended Data Fig. 7 | HRAS and NRAS directly interact with KRAS<sup>G12D</sup>.**

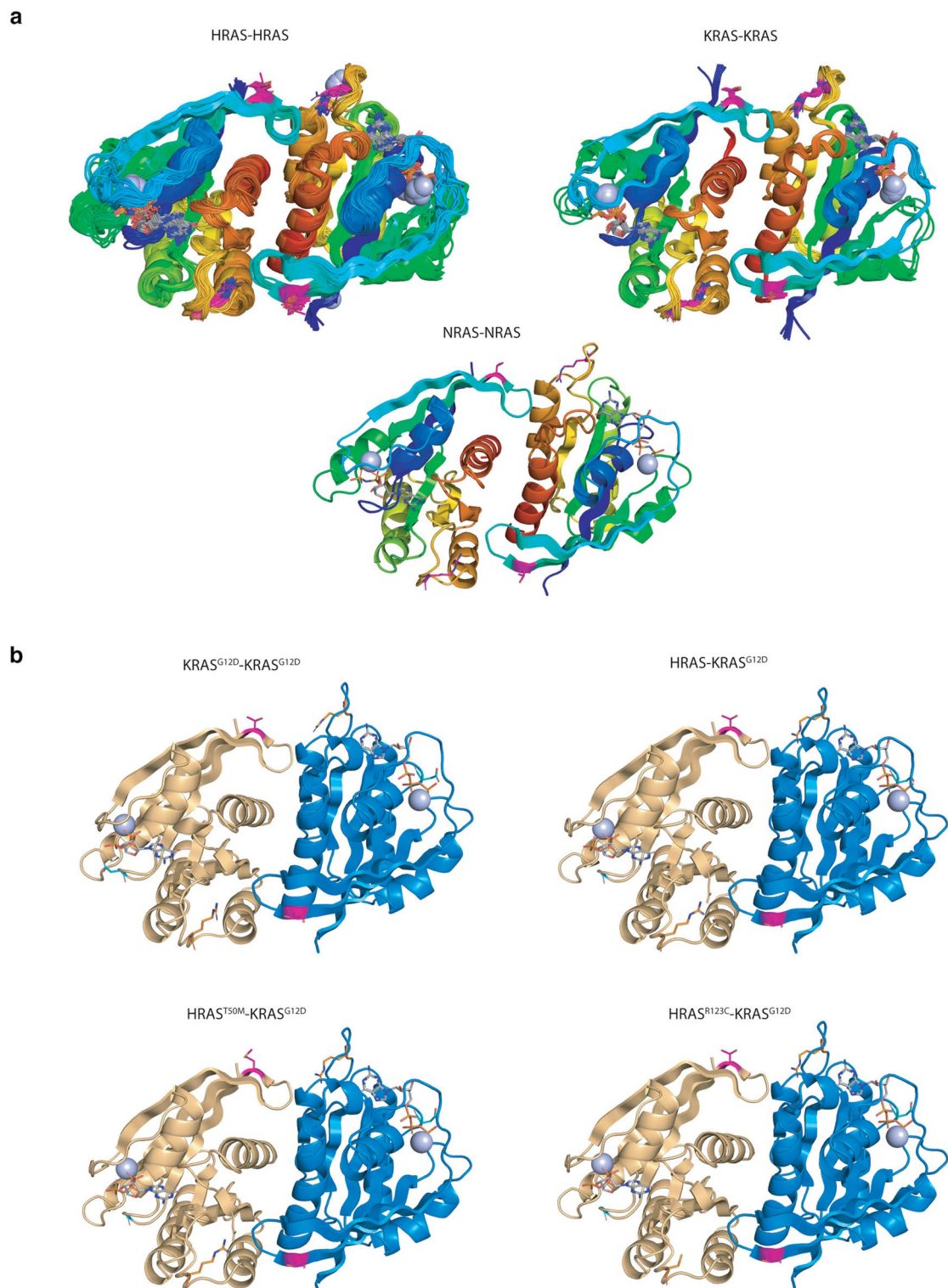
**a.** Co-immunoprecipitation of HRAS (HA-tagged) and NRAS (Flag-tagged) with KRAS<sup>G12D</sup> (Myc-tagged), imaged by western blotting. 293T cells were co-transfected with Myc-KRAS<sup>G12D</sup>, HA-HRAS, and Flag-NRAS for 24 hours before co-immunoprecipitation. **b.** Co-immunoprecipitation of HRAS (HA-tagged) with truncated (aa73-aa165) or full length KRAS<sup>G12D</sup> (Myc-tagged), imaged by western blotting. 293T cells were co-transfected with Myc-KRAS<sup>G12D</sup> and HA-HRAS for 24 hrs before co-immunoprecipitation. **c.** Diagram of the modified ReBiL2.0 system to assess direct KRAS<sup>G12D</sup>-HRAS/NRAS interaction. **d.** HRAS and NRAS can directly interact with KRAS<sup>G12D</sup>. 293 T cells expressing indicated cLuc- and nLuc- luciferase were cultured in limited serum (1%) for 24 hours and ReBiL2.0 assay was performed. Points are Mean±SD ReBiL2.0 score of 12 wells normalized to cells expressing free luciferase (cLuc-HA/nLuc-HA). (one-way ANOVA). **e.** Luciferase protein expression in **c**, imaged by western blotting for the HA-tag.  $\alpha$ -Tubulin is loading control. **f.** Full data from experiment shown in Fig. 5c. 293T cells

expressing nLuc-KRAS<sup>G12D</sup>/cLuc-KRAS<sup>G12D</sup> or nLuc-C20/cLuc-C20 with indicated Myc-tagged RAS-GTPases were cultured in limited serum (1%) for 24 hours and ReBiL2.0 assays were performed. Points are Mean±SD ReBiL2.0 score of 12 wells normalized to cells transduced with empty vector. ns: not significant (one-way ANOVA). **g.** RAS-GTPases protein expression in **e**, imaged by western blotting for the Myc-tag. HSP90 is loading control. **h.** Relative strength of RAS-GTPases in disrupting KRAS<sup>G12D</sup>-KRAS<sup>G12D</sup> interactions in **f**. Differences in ReBiL2.0 score between empty vector and indicated RAS-GTPases were normalized by their own protein expression via western blotting for the Myc-tag. (one-way ANOVA). **i.** RAPIA interacts with KRAS<sup>G12D</sup> in two protein-protein interaction analyses (Kelly, Kostyrko, Han *et al.* 2020; Broyde, Simpson, Murray *et al.* 2020). **j.** Co-immunoprecipitation of BRAF with KRAS<sup>G12D</sup> (Myc-tagged), imaged by western blotting. 293T cells were co-transfected with Myc-KRAS<sup>G12D</sup>, BRAF, and with or without HA-HRAS for 24 hours before co-immunoprecipitation. Overexpression (OvE) of HRAS suppressed BRAF co-immunoprecipitation with KRAS<sup>G12D</sup>.



**Extended Data Fig. 8 | Identification and analysis of rare RAS mutations in oncogenic KRAS-mutant tumors. a-b.** Pan-cancer frequency of HRAS (a) or NRAS (b) mutations in patients from Project GENIE. Mutations that are intergenic, intronic, silent, or in the 3' or 5' UTR were excluded. Oncogenic KRAS mutants were defined as tumors having missense mutations in codons 12, 13 or 61. Known oncogenic HRAS (a) or NRAS (b) mutations are highlighted. The dashed line indicates equal mutation frequency in samples with wild-type and mutant KRAS. Non-oncogenic mutations occurring at least once in patients with oncogenic KRAS mutations are annotated. Mutants selected for analysis of ability to disrupt KRAS<sup>G12D</sup>-KRAS<sup>G12D</sup> interactions are in bold. **c-d.** Characteristics of samples with rare HRAS (c) or NRAS (d) mutations selected for analysis of ability to disrupt KRAS<sup>G12D</sup>-KRAS<sup>G12D</sup> interactions using the ReBiL2.0 system. **e.** Identification of RAS-RAS interaction-deficient NRAS mutation. 293 T (nluc-KRAS<sup>G12D</sup>/cluc-KRAS<sup>G12D</sup>) cells expressing wild-type or NRAS mutants were cultured in limited serum (1%) for 24 hours. Points are Mean±SD ReBiL2.0 score

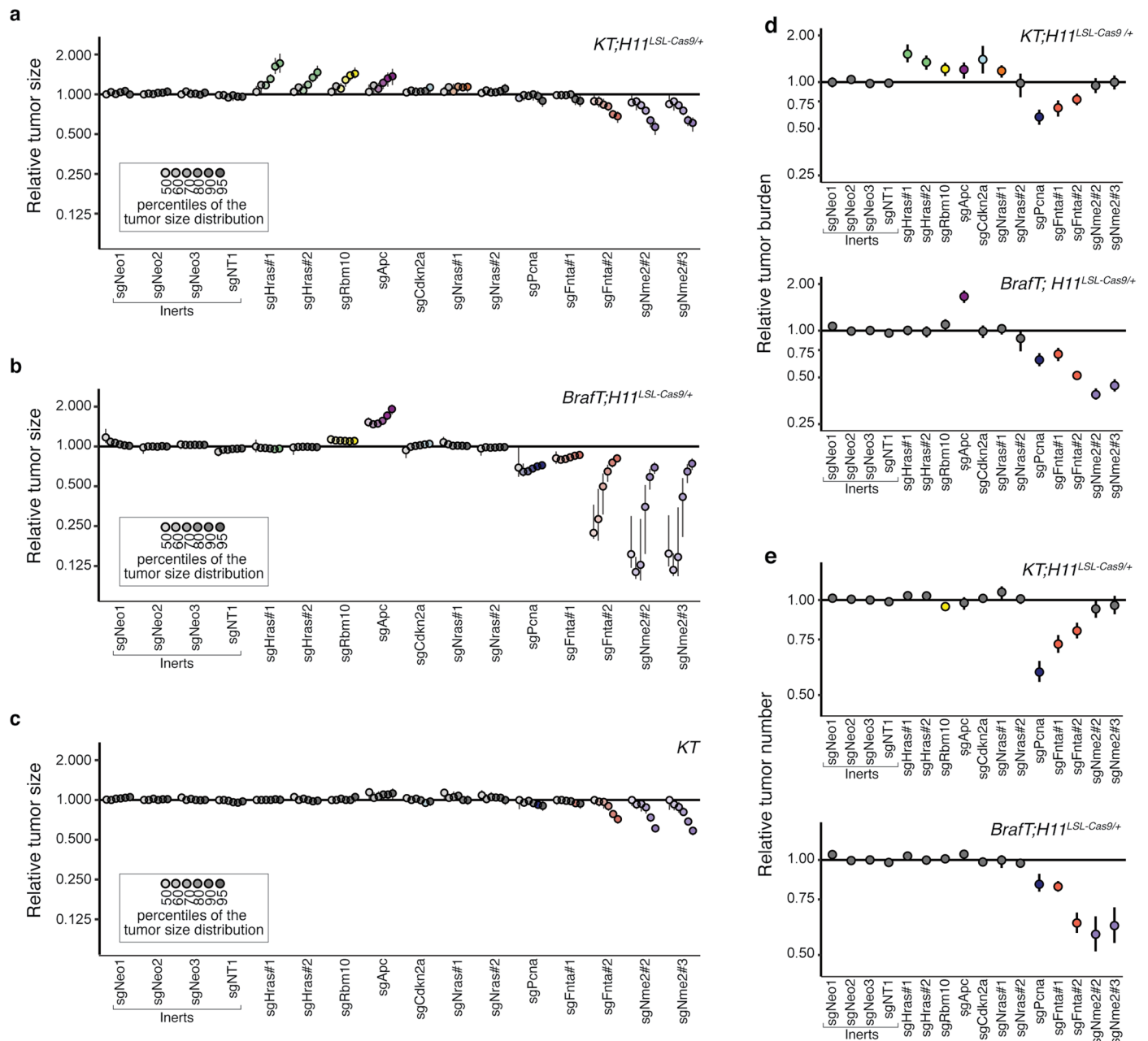
of 12 wells normalized to cells transfected with empty vector. ns: not significant (one-way ANOVA). **f.** NRAS (wild-type and mutant) protein expression levels in a shown by anti-Myc tag western blot. HSP90 is loading control. **g.** Western blot of cultured NRAS-null HOP62 cells (HOP62-Cas9-sgNRAS) re-expressing sgRNA-resistant wild-type NRAS or NRAS<sup>R102Q</sup> under Dox treatment. Cells were cultured under limited serum (1%) with or without Dox for 2 days before protein extraction. Re-expression of NRAS<sup>R102Q</sup> had no effect on ERK phosphorylation. GAPDH is loading control. **h.** Proliferation of cultured NRAS-null HOP62 cells (HOP62-Cas9-sgNRAS) expressing sgRNA-resistant wild-type NRAS or NRAS<sup>R102Q</sup> under Dox treatment. Cells were cultured in limited serum (1%) with or without Dox for 4 days. Cell viability was measured via CCK8 assay and normalized to cells treated with vehicle. Re-expression of NRAS<sup>R102Q</sup> had no effect on cell proliferation. Points are Mean±SD of 10 wells. ns: not significant (one-tailed t-test).



**Extended Data Fig. 9 | Prediction of RAS-RAS dimer interfaces. a.**

Homodimers of RAS present in crystals of HRAS, KRAS, and NRAS in the Protein Data Bank. Dimers were downloaded from the Protein Common Interface Database (ProtCID)<sup>58</sup>, which clusters interfaces present in different crystals of homologous proteins. The  $\alpha$ 4- $\alpha$ 5 dimer shown is present in 84 entries of HRAS, 13 entries of KRAS, and one entry of NRAS (PDB 5UHV). **b.** Models of a homodimer of KRAS<sup>G12D</sup> and heterodimers of KRAS<sup>G12D</sup> with HRAS, HRAS<sup>T50M</sup>, and HRAS<sup>R123C</sup>. The  $\alpha$ 4- $\alpha$ 5 HRAS dimer from PDB entry 3K8Y was used as a template. KRAS<sup>G12D</sup> from PDB entry 5USJ was superposed with the program PyMol on one or both monomers of 3K8Y to form the heterodimers and the homodimer respectively.

Residues T50 and R123 were mutated with PyMol. R123 is involved in an intrachain salt bridge with residue E143, which also participates in the RAS-RAS interface. Mutation to cysteine results in an uncompensated charge on E143, which may destabilize the RAS-RAS interaction. All four structures were relaxed with the program Rosetta using the FastRelax protocol with the Ref2015 scoring function<sup>59</sup>. Rosetta uses the backbone-dependent rotamer library of Shapovalov and Dunbrack to repack side chains around the mutated sites<sup>60</sup>. The resulting energies were: KRAS<sup>G12D</sup>-KRAS<sup>G12D</sup>, -1122.8 kcal/mol; HRAS-KRAS<sup>G12D</sup>, -1144.8 kcal/mol; HRAS<sup>T50M</sup>-KRAS<sup>G12D</sup>, -1135.5 kcal/mol; HRAS<sup>R123C</sup>-KRAS<sup>G12D</sup>, -1130.9 kcal/mol. Residues T50 (magenta) and R123 (orange) are indicated in sticks.



**Extended Data Fig. 10 | Paired screen in KRAS-driven and BRAF-driven lung cancer models validates HRAS and NRAS as KRAS-specific tumor suppressors. a-c.** Points denote tumor sizes at indicated percentiles for each sgRNA relative to the size of sgInert-containing tumors at the corresponding percentiles in *KT;H11<sup>LSL-Cas9/+</sup>* (**a**), *BraffT;H11<sup>LSL-Cas9/+</sup>* (**b**) and *KT* mice (**c**). Genes are ordered by 95<sup>th</sup> percentile tumor size in *KT;H11<sup>LSL-Cas9/+</sup>* mice, with sgInerts on the left. Percentiles that are significantly different from sgInert (two-sided FDR-adjusted  $p < 0.05$ ) are in color. The negative effects of sgRNAs targeting *Fnta* and *Nme2* in the *KT* mice (**c**) are unexpected and indicate a potential bias in the size distributions of tumors with these genotypes. We note that the same bias may be present in the *KT;H11<sup>LSL-Cas9/+</sup>* and *BraffT;H11<sup>LSL-Cas9/+</sup>* data; however, previous experiments showed consistent negative effects on tumor size for these sgRNAs, suggesting that the observed effects in this *KT;H11<sup>LSL-Cas9/+</sup>* cohort are not solely the product of this bias. **d.** Points denote the impact of each sgRNA on tumor burden

relative to sgInerts in *KT;H11<sup>LSL-Cas9/+</sup>* and *BraffT;H11<sup>LSL-Cas9/+</sup>* mice, normalized to the corresponding statistic in *KT* mice to account for representation of each sgRNA in the viral pool. Relative tumor burdens significantly different from sgInert (two-sided FDR-adjusted  $p < 0.05$ ) are in color. **e.** Points denote the impact of each sgRNA on tumor number relative to sgInerts in *KT;H11<sup>LSL-Cas9/+</sup>* and *BraffT;H11<sup>LSL-Cas9/+</sup>* mice, normalized to the corresponding statistic in *KT* mice to account for representation of each sgRNA in the viral pool. Relative tumor numbers significantly different from sgInert (two-sided FDR-adjusted  $p < 0.05$ ) are in color. For all panels: Error bars indicate 95% confidence intervals around point estimates of the test statistic. sgInerts are in gray and the line at  $y = 1$  indicates no effect relative to sgInerts. Confidence intervals and P-values were calculated using the nested bootstrap resampling approach described in the Methods across 11 *KT;H11<sup>LSL-Cas9/+</sup>* mice, 14 *BraffT;H11<sup>LSL-Cas9/+</sup>* mice and 10 *KT* mice.

## Reporting Summary

Nature Research wishes to improve the reproducibility of the work that we publish. This form provides structure for consistency and transparency in reporting. For further information on Nature Research policies, see our [Editorial Policies](#) and the [Editorial Policy Checklist](#).

### Statistics

For all statistical analyses, confirm that the following items are present in the figure legend, table legend, main text, or Methods section.

n/a Confirmed

- The exact sample size ( $n$ ) for each experimental group/condition, given as a discrete number and unit of measurement
- A statement on whether measurements were taken from distinct samples or whether the same sample was measured repeatedly
- The statistical test(s) used AND whether they are one- or two-sided  
*Only common tests should be described solely by name; describe more complex techniques in the Methods section.*
- A description of all covariates tested
- A description of any assumptions or corrections, such as tests of normality and adjustment for multiple comparisons
- A full description of the statistical parameters including central tendency (e.g. means) or other basic estimates (e.g. regression coefficient) AND variation (e.g. standard deviation) or associated estimates of uncertainty (e.g. confidence intervals)
- For null hypothesis testing, the test statistic (e.g.  $F$ ,  $t$ ,  $r$ ) with confidence intervals, effect sizes, degrees of freedom and  $P$  value noted  
*Give  $P$  values as exact values whenever suitable.*
- For Bayesian analysis, information on the choice of priors and Markov chain Monte Carlo settings
- For hierarchical and complex designs, identification of the appropriate level for tests and full reporting of outcomes
- Estimates of effect sizes (e.g. Cohen's  $d$ , Pearson's  $r$ ), indicating how they were calculated

*Our web collection on [statistics for biologists](#) contains articles on many of the points above.*

### Software and code

Policy information about [availability of computer code](#)

Data collection No software was used to collect the data

Data analysis Python 3.4 was used for all analyses of barcode sequencing data. GraphPad Prism 9 and R 3.6.0 were used for data visualization. ImageJ 1.52p was used for histology image data analysis. Pymol 2.4 and Rosetta were used for protein modeling. Code used for the analysis of barcode sequencing data in this study is now publicly available on GitHub (<https://github.com/eshuldiner/KrasIP>). All other custom code used in this study is available upon request.

For manuscripts utilizing custom algorithms or software that are central to the research but not yet described in published literature, software must be made available to editors and reviewers. We strongly encourage code deposition in a community repository (e.g. GitHub). See the Nature Research [guidelines for submitting code & software](#) for further information.

### Data

Policy information about [availability of data](#)

All manuscripts must include a [data availability statement](#). This statement should provide the following information, where applicable:

- Accession codes, unique identifiers, or web links for publicly available datasets
- A list of figures that have associated raw data
- A description of any restrictions on data availability

The human cancer genomic data analyzed in this manuscript were derived from the AACR's Project GENIE (<https://www.aacr.org/professionals/research/aacr-project-genie/>) Release 9.1-public dataset, and from the TCGA PanCancer Atlas dataset. All data files from Project GENIE that support the findings of this study are available through the Synapse platform (<https://www.synapse.org/#!Synapse:syn24179657>). All data files from the TCGA PanCancer Atlas dataset are accessible through the cBioPortal ([https://www.cbioportal.org/study/summary?id=luad\\_tcga\\_pan\\_can\\_atlas\\_2018](https://www.cbioportal.org/study/summary?id=luad_tcga_pan_can_atlas_2018)). The protein templates used to model RAS heterodimers in

this study are available through the ProtCID database (KRAS-G12D: PDB entry 5USJ, HRAS homodimer: PDB entry 3K8Y), and resulting structural data files can be accessed through zenodo (<https://zenodo.org/record/7104280>). AP/MS data were derived from Kelly, Kostyko, Han et al. 2020 (PMID: 32727735, Supplemental Table 2) and Broyde, Simpson, Murray et al. 2020 (PMID: 32929263 Supplementary File 3). Gene expression data were derived from Chuang et al. 2017 (PMID: 28191885; Supplemental Table 1). Pre-existing CRISPR/Cas9 screen data were derived from Han et al. 2020 (PMID: 32238925, Supplementary Table 4).

All barcode sequencing datasets are available through the NCBI's Sequence Read Archive database under the BioProject accession number PRJNA763983 (<https://www.ncbi.nlm.nih.gov/sra/PRJNA763983>). All figures have associated raw data. Data for Figures 1-6 and Extended Figures 1-8, 10 have been available in the Extended Data; data associated with Extended Figure 9 is available at <https://zenodo.org/record/7104280>. All other data supporting the findings of this study are available from the corresponding author on reasonable request.

## Field-specific reporting

Please select the one below that is the best fit for your research. If you are not sure, read the appropriate sections before making your selection.

Life sciences  Behavioural & social sciences  Ecological, evolutionary & environmental sciences

For a reference copy of the document with all sections, see [nature.com/documents/nr-reporting-summary-flat.pdf](https://nature.com/documents/nr-reporting-summary-flat.pdf)

## Life sciences study design

All studies must disclose on these points even when the disclosure is negative.

Sample size	Sample size was determined based on our previous experience and power calculations. (Rogers, McFarland, Winters et al. Nature Genetics, 2018; Cai, Chew, Li et al. Cancer Discovery, 2021)
Data exclusions	No data is excluded in this study.
Replication	We performed extensive technical (2-3 sgRNAs for each target) and biological replications (> 5 mice for each cohort, >8 wells per culture condition) of the experiments as detailed in the manuscript. For cell culture experiments, we performed 3 independent experiments and representative results are shown. Our findings are consistent across replicates.
Randomization	Formal sample randomization was not performed in this study. However, we allocated mice to ensure that all experimental cohorts were sex balanced and had similar distributions of ages, thereby controlling for these covariates.
Blinding	For reasons of practicality, experiments were not blinded during mouse handling and analyses that required directly handling samples. Downstream analyses of barcode sequencing data were performed using a pre-existing pipeline that was applied identically to all samples; thus we do not anticipate these steps introducing bias.

## Reporting for specific materials, systems and methods

We require information from authors about some types of materials, experimental systems and methods used in many studies. Here, indicate whether each material, system or method listed is relevant to your study. If you are not sure if a list item applies to your research, read the appropriate section before selecting a response.

### Materials & experimental systems

### Methods

n/a	Involved in the study
<input type="checkbox"/>	<input checked="" type="checkbox"/> Antibodies
<input type="checkbox"/>	<input checked="" type="checkbox"/> Eukaryotic cell lines
<input checked="" type="checkbox"/>	<input type="checkbox"/> Palaeontology and archaeology
<input type="checkbox"/>	<input checked="" type="checkbox"/> Animals and other organisms
<input checked="" type="checkbox"/>	<input type="checkbox"/> Human research participants
<input checked="" type="checkbox"/>	<input type="checkbox"/> Clinical data
<input checked="" type="checkbox"/>	<input type="checkbox"/> Dual use research of concern

n/a	Involved in the study
<input checked="" type="checkbox"/>	<input type="checkbox"/> ChIP-seq
<input checked="" type="checkbox"/>	<input type="checkbox"/> Flow cytometry
<input checked="" type="checkbox"/>	<input type="checkbox"/> MRI-based neuroimaging

## Antibodies

Antibodies used	HSP90 (BD Biosciences, 610418), pAKT (Cell Signaling, 4060S), pERK (Cell Signaling, 4370L), ERK (Cell Signaling, 9102S), AKT (Cell Signaling, 4691S), HRAS (Thermo Fisher Scientific, 18295-1-AP), NRAS (Santa Cruz Biotechnology, sc-31), KRAS (EMD Millipore, OP-24), HA-tag (Cell Signaling, 2999S), Myc-tag (Cell Signaling, 2040S), Flag-tag (Cell Signaling, 86861S), BRAF (Cell Signaling, 14814S), $\alpha$ -Tubulin (Cell Signaling, 2144S), GAPDH (Cell Signaling, 5174S), Ki-67 (BD Biosciences, 550609), Goat-anti-Rabbit IgG Antibody, HRP-conjugate (Sigma-Aldrich, 12-348), Goat-anti-Mouse IgG Antibody, HRP-conjugate (Thermo Fisher Scientific, 62-6520)
Validation	HSP90, Ki-67, BrdU antibodies have been validated in previous projects from our lab. (Murray et al. 2019) pAKT, pERK antibodies have been validated in previous publications (e.g. Cicchini et al. 2017)

